Monthly Notices of the ROYAL ASTRONOMICAL SOCIETY

MNRAS **547,** 1–28 (2026)
Advance Access publication 2026 January 30

https://doi.org/10.1093/mnras/stag210

When relics were made: vigorous stellar rotation and low dark matter content in the massive ultra-compact galaxy GS-9209 at $z = 4.66$

Robert G. Pascalau [1,2★] Francesco D'Eugenio [1,2★] Sandro Tacchella [1,2] Roberto Maiolino [1,2,3] Michele Cappellari [4] Qiao Duan [1,2] Claudia del P. Lagos [5,6] Andrew J. Bunker [4] Gareth C. Jones [1,2,4] Jan Scholtz [1,2] Hannah Übler [7] Giovanni Cresci [8] Santiago Arribas [9] Michele Perna [9] Arjen van der Wel [10,11] A. Lola Danhaive [1,2] William McClymont [1,2] Christina C. Williams,[12,13] Anna de Graaff [11] Akash Vani [14,15] Michael V. Maseda [16] Adam C. Carnall [17] Stéphane Charlot [18] Stefano Carniani [19] Tze P. Goh [1,2] Zhiyuan Ji [13] and Pablo Pérez González [9]

Affiliations are listed at the end of the paper

Accepted 2026 January 28. Received 2026 January 21; in original form 2025 May 13

ABSTRACT

James Webb Space Telescope (*JWST*) uncovered a large number of massive quiescent galaxies (MQGs) at $z > 3$, which theoretical models struggle to reproduce. Explaining the number density of such objects requires extremely high conversion efficiency of baryons into stars in early dark matter haloes. Using stellar kinematics, we can investigate the processes shaping the mass assembly histories of MQGs. We present high-resolution *JWST*/NIRSpec integral field spectroscopy of GS-9209, a massive compact quiescent galaxy at $z = 4.66$ ($\log(M_*/\mathrm{M}_\odot) = 10.52 \pm 0.06$, $R_{\rm eff} = 220 \pm 20$ pc). Full spectral fitting of the spatially resolved stellar continuum reveals a clear rotational pattern, yielding a spin parameter of $\lambda_{2R_{\rm eff}} = 0.85 \pm 0.10$. This study suggests that at least a fraction of the earliest quiescent galaxies were fast rotators and that quenching was a dynamically gentle process, preserving the stellar disc even in highly compact objects. Using Jeans anisotropic modelling and assuming a Navarro–Frenk–White profile, we measure a dark matter fraction of $f_{\rm DM}(< 2R_{\rm eff}) = 14.5^{+6.0}_{-4.2}$ per cent. Our findings use stellar kinematics to confirm the massive nature of early quiescent galaxies, previously inferred from stellar population modelling. We suggest that GS-9209 has a similar structure to low-redshift 'relic' galaxies. However, unlike relic galaxies, which have bottom-heavy initial mass functions (IMF), the dynamically inferred stellar mass-to-light ratio of GS-9209 is consistent with a Milky Way-like IMF. The kinematical properties of GS-9209 are different from those of $z < 1$ early-type galaxies and more similar to those of recently quenched post-starburst galaxies at $z > 2$.

Key words: galaxies: evolution – galaxies: formation – galaxies: kinematics and dynamics – galaxies: structure.

1 INTRODUCTION

Galaxies' star formation histories (SFHs) and observed stellar populations are fundamental to our understanding of galaxy evolution. The star formation activity of a galaxy is closely related to its morphology (as it was revealed by studies on $0 < z < 2.5$ galaxies e.g. R. Brennan et al. 2017; P. Dimauro et al. 2022). A further link exists between galactic morphologies and kinematics with the classical paradigm splitting the galaxies population into rotationally supported flattened discs and dispersion-supported spheroids (E. Emsellem et al. 2007, 2011; M. T. Graham et al. 2018; J. de Sande et al. 2018; A. C. R. Thob et al. 2019). Such classifications seem to be valid up to a redshift of $z \sim 3$ (e.g. R. Brennan et al. 2017) but it is unclear whether they hold true for higher z galaxies (R. G. Abraham 1999).

The question of how different types of galaxies are born, evolve, and end up being 'red and dead' has been central in our quest to understand galactic evolution. Since the star formation rate (SFR) is a key property of any galaxy, it goes without saying that quenching also has a dramatic impact on the evolution of both individual systems and the galaxy population as a whole. There is a wide variety of quenching mechanisms at play, depending on galaxy's stellar mass, kinematics, and on its environment (A. Man & S. Belli 2018; A. F. L. Bluck et al. 2020a, b; L. Cortese, B. Catinella & R. Smith 2021). A few examples include removal of cold molecular gas via outflows driven by active galactic nuclei (AGNs; e.g. A. Fluetsch & others 2019; S. Veilleux & others 2020), ram pressure stripping (the main mechanism in the case of low-mass galaxies; J. E. Gunn & J. R. Gott 1972), or strangulation in the case of more massive galaxies (a complete halt

★ E-mail: rgp34@cam.ac.uk (RGP); fdeugenio@gmail.com (FDE)

of the galaxy's pristine gas inflows, Y. Peng & others 2015). The latter is often the result of the halo heating due to supermassive black hole (SMBH) feedback (J. Silk & M. J. Rees 1998; R. G. Bower & others 2006; D. J. Croton & others 2006; C. D. P. Lagos, S. A. Cora & N. D. Padilla 2008; S. Brownson & others 2019) but the gas might also get heated when falling into the dark matter haloes' gravitational potential (virial shock heating; S. D. M. White & M. J. Rees 1978; D. Kereš et al. 2005; A. Dekel & Y. Birnboim 2006). Star formation quenching is an important process in the evolution of galaxies, having a crucial effect on their subsequent morphologies. Furthermore, there is a strong correlation between a galaxy's average stellar population age and its morphology (M. R. Blanton & J. Moustakas 2009; R. S. Somerville & R. Davé 2015) or kinematics (S. M. Croom et al. 2024).

Since the launch of *James Webb Space Telescope* (*JWST*; J. P. Gardner et al. 2023; J. Rigby et al. 2023) the sample of high-z massive quiescent galaxies (MQGs) has seen a dramatic increase in the number of studies on confirmed spectroscopic candidates in the redshift range $3 < z < 5$ (A. C. Carnall et al. 2023a, b, 2024; F. Valentino et al. 2023; F. D'Eugenio et al. 2024; A. Graaff et al. 2024; T. Nanayakkara et al. 2024; D. J. Setton et al. 2024; W. M. Baker et al. 2025a; P. G. Pérez-González et al. 2025) even going as early as $z \sim 7.3$ (A. Weibel et al. 2025). These observations imply much higher number densities of MQGs compared with the predictions from numerical simulations or semi-analytic models (e.g. *TNG300* – A. I. Hartley et al. 2023; *Magneticum Pathfinder* – L. C. Kimmig et al. 2025; *FLARES* – C. C. Lovell et al. 2023; *SHARK v2.0* – C. d. P. Lagos et al. 2024; *FLAMINGO* – W. M. Baker et al. 2025a; *L-Galaxies* – A. Vani et al. 2025). C. d. P. Lagos et al. (2025) analysed six large cosmological simulations (three semi-analytic models: GAEA, GALFORM, and SHARK and three full hydro-dynamical simulations: SIMBA, EAGLE, and IllustrisTNG) and showed that these simulations predict that the number densities of $z \sim 4.5$ MQGs ($M_* > 10^{10.5}$ M$_\odot$, sSFR < 0.1 Gyr^{-1}) are smaller than measured from *JWST* observations, the difference ranging from 1.5 to 3 dex depending on the simulation. Furthermore, it was demonstrated that the simulations are unable to reproduce the observed stellar mass functions of quiescent galaxies at $2 < z < 5$, as demonstrated by W. M. Baker et al. (2025b).

Even more puzzlingly, high-redshift MQGs appear to have assembled large stellar masses ($M_* > 10^{10}$ M$_\odot$) during intense star formation episodes (up to 2000 M$_\odot$ yr^{-1} or more, B. Forrest et al. 2020) and then quench extremely rapidly in comparison to their local counterparts (D. Thomas et al. 2010; R. M. McDermid et al. 2015). Many observational studies have focused on the SFHs of these galaxies, but the processes governing their mass assembly history and quenching remain covered in mystery. MQGs pose at least three major challenges for current models of galaxy formation and evolution, resulting from (1) their unexpected high number densities at high redshift (e.g. A. C. Carnall et al. 2023b; F. Valentino et al. 2023; S. Alberts et al. 2024; A. S. Long et al. 2024; Y. Zhang et al. 2025), (2) their high stellar mass (possibly related to the high efficiency of baryon conversion into stars in high-redshift massive haloes, e.g. A. Dekel et al. 2023), and (3) the rapid quenching mechanism. Within the standard paradigm of galaxy formation, the star formation and quenching time-scales of MQGs imply the existence of impossibly massive haloes at early times (e.g. K. Glazebrook et al. 2024; C. Turner et al. 2025; A. Weibel et al. 2025).

Continued star formation from the available cold gas would be more problematic, giving rise to impossibly massive galaxies, which would be inconsistent with both observations (R. G. Bower, A. J. Benson & R. A. Crain 2012; C. M. Harrison et al. 2018) and with the low-redshift stellar mass function extrapolation (D. J. McLeod et al. 2021). Therefore, another issue to be discussed is the fast quenching time-scale of high-z MQGs given the early stage of the Universe when dark matter haloes are accreting gas at extremely high rates (S. Tacchella et al. 2018). These conditions point towards the possible responsible quenching mechanism being AGN ejective feedback (J. Silk & M. J. Rees 1998; T. Di Matteo, V. Springel & L. Hernquist 2005; R. Maiolino et al. 2012; S. Belli et al. 2024; L. Xie et al. 2024; S. Lim et al. 2025) as significantly more violent and more rapid than other quenching mechanisms (S. Tacchella et al. 2022). In fact, about 50 per cent of MQGs at $1.5 < z < 4.5$ are AGN hosts (W. M. Baker et al. 2025a; L. Bugiani et al. 2025). Furthermore, these claims of AGN feedback being responsible for quenching high-z MQGs are backed-up by theoretical studies such as J. M. Piotrowska et al. (2022) or C. d. P. Lagos et al. (2025). Other theoretical works discuss possible alternative processes leading to a rapid gas consumption in MQGs, such as violent disc instabilities or feedback free star formation (A. Dekel et al. 2023; A. Vani et al. 2025).

Indeed, many previous studies on MQGs show them to have low amounts of cold gas, the fuel star formation ($f_{\rm gas} = M_{\rm gas}/\left(M_{\rm gas} + M_*\right) < 20$ per cent; e.g. S. Belli et al. 2021; K. E. Whitaker et al. 2021; C. C. Williams et al. 2021; C. Woodrum et al. 2022; J. Scholtz et al. 2024). However, other studies confirm the presence of non-negligible cold molecular gas reservoir that MQGs are unable to use for star formation. This is seen at various redshifts: $z \sim 0$ (K. Rowlands et al. 2015) and $z \sim 1$ (R. Bezanson et al. 2022). The latter study reveals the extremely short cold gas depletion time-scales ($\sim$ 100-200 Myr) of recently quenched galaxies, interpreting this result as a possible evidence of AGN feedback. These studies highlight the contrast between the population of old quiescent galaxies and the ones who stopped forming stars more recently (post-starburst galaxies, PSBs). A similar classification of high-redshift MQGs has emerged from studies of their SFHs (M. Park et al. 2024). In contrast to PSBs, the cold gas fractions of galaxies quenched long before the observation time (> 1 Gyr) is more difficult to interpret. Using a sample of $z \sim 0.7$ MQGs, C. Woodrum et al. (2022) find evidence for post-quenching rejuvenation effects driven by gas-rich minor mergers. However, K. A. Suess et al. (2023) found that the less massive, but more highly star-forming satellites of MQGs, although they do not necessarily bring substantial amounts of cold gas, they can contribute (via minor mergers) to up to 30 per cent of the central galaxies stellar mass.

In this paper, we present high-resolution $R \sim 2700$ NIRSpec integral-field-unit (IFU) observations of the massive quenched galaxy GS-9209 at redshift $z = 4.66$, whose SFH and various structural and morphological properties (size, central BH, AGN properties, stellar and dust SED) have been studied in depth in A. C. Carnall et al. (2023b) and Z. Ji et al. (2024b). With the unique ability of NIRSpec/IFU to provide both complete spatial and spectral information, we focus here on the kinematical and dynamical characterization of this MQG. This is the earliest quiescent system for which an IFU study is conducted (revealing an ordered rotational pattern in V_*, the first moment of the line-of-sight velocity distribution). Integral-field spectroscopy is necessary because it can distinguish between the types of AGN

feedback that played a major role in quenching GS-9209: ejective feedback (expelling much of the cold gas out into the CGM before it gets the chance of collapsing into stars, e.g. P. F. Hopkins et al. 2008; C. Feruglio et al. 2010; R. Maiolino et al. 2012) versus preventative feedback (which does not allow new cold gas to be accreted by the galaxy usually due to halo heating, e.g. R. G. Bower et al. 2006; S. Brownson et al. 2019). A possible kinematic parameter that can potentially give us insights about the type of AGN feedback in a galaxy's history is $(V/\sigma)_{R_{\rm eff}}$, the ratio between ordered stellar rotation and random motions, within the half-light radius ($R_{\rm eff}$). In the case of high-redshift star-forming discs we have that $(V/\sigma)_{R_{\rm eff}} > 1$ (N. M. Förster Schreiber & S. Wuyts 2020). Galaxies that show a disc-like rotational kinematic pattern in V_* but have, in the same time, $(V/\sigma)_{R_{\rm eff}}$ values lower than 1 could potentially indicate a violent, ejective AGN feedback in galaxy's history, whereas galaxies that have $(V/\sigma)_{R_{\rm eff}} \sim$ 1.5-2 are more likely to be associated with a gentle mode of AGN feedback (preventative).

This paper is structured as follows: in Section 2, we discuss the general data analysis and data reduction pipeline, outlining the pre-processing that we have done on raw data before using it in our analysis. Section 3 discusses the computational and mathematical tools that we have used to analyse the photometry data and perform Multi-Gaussian expansion (MGE) parametrization, as well as spectrum fitting and Voronoi binning, vital in deriving the subsequent resolved kinematics maps. In Section 4, we dedicate separate subsections to various important key results that highlight different properties of GS-9209. We discuss the implications for galaxy formation and evolution models and compare our results with those from independent observations in Section 5. Our findings are summarized in Section 6, where we also give possible directions where further research might give precious insights. Throughout this paper, we adopt a flat universe cosmology with matter density parameter $\Omega_{\rm m} = 0.307$ and Hubble Constant $\rm H_0 = 67.7\ km\ s^{-1}\ Mpc^{-1}$ as in Planck Collaboration VI (2020). We use the AB magnitude system.

2 DATA

The data we use were obtained as part of the *JWST* Cycle 2 Program ID 3659 (PI: Francesco D'Eugenio). This is a NIRSpec (P. Jakobsen et al. 2022) IFU programme (T. Böker et al. 2022) and the observations use the high-resolution ($R \sim 2700$) disperser/filter combinations G235H/F170LP and G395H/F290LP. In this work we focus on G235H/F170LP, which was integrated for 14.7 h, using 18 dithered observations in a nine-point medium-sized cycling pattern (repeated twice). Each dither consisted of 20 groups per integration and two integrations, using the NRSIRS2 readout mode (B. J. Rauscher et al. 2017). The medium-size dither pattern gives an effective field of view (FoV) of our particular observation of 101 × 91 spaxels with a resolution of 0.05 arcsec per spaxel. The NIRSpec FoV is displayed in Fig. 1 (dotted rectangle), superimposed to a false-colour NIRCam image. At the redshift $z \sim 4.658$ of our target, we probe a rest-frame wavelength range $\lambda_{\rm rest} \in [2934\text{Å}; 5603\text{Å}]$ with the detector gap between 4220 and 4310 Å (rest-frame wavelengths; see Fig. 2).

2.1 Data reduction and background subtraction

We used the publicly available *JWST* data reduction pipeline v1.12.5, with calibration files from the context file 1193. The standard pipeline was complemented by customized methods for

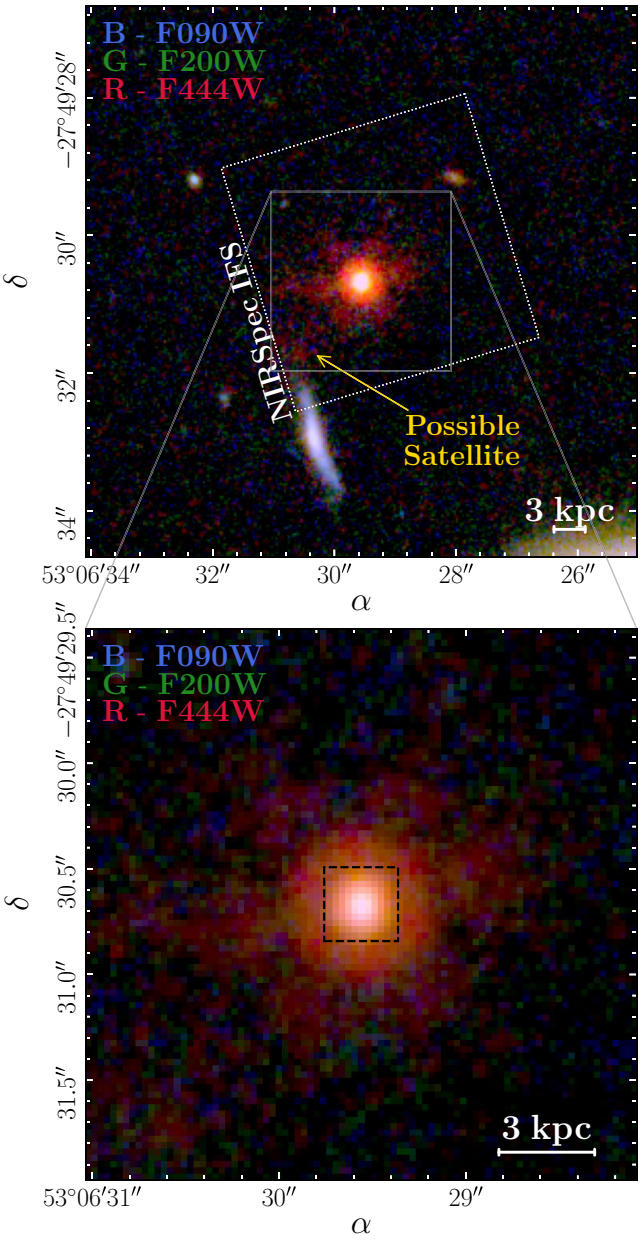

Figure 1. Top panel: composite image of GS-9209 obtained by the superposition of *F090W*, *F200W*, and *F444W* NIRCam photometry images. The dotted line is the effective FoV of our NIRSpec observations. A possible satellite is indicated. **Bottom panel:** zoomed-in portion of the same image, where we highlight the 0.35 arcsec × 0.35 arcsec aperture used for measuring the integrated stellar velocity dispersion σ'_*.

snowball flagging, pink-noise correction, and outlier detection, as described in M. Perna et al. (2023).

2.1.1 Source detection

We used the package SEP[1] (Source Extraction and Photometry Python library). This first normalizes the original image and subtracts a crude estimate for the background (SEP.BACKGROUND)

[1] Available at https://sep.readthedocs.io/en/v1.1.x/

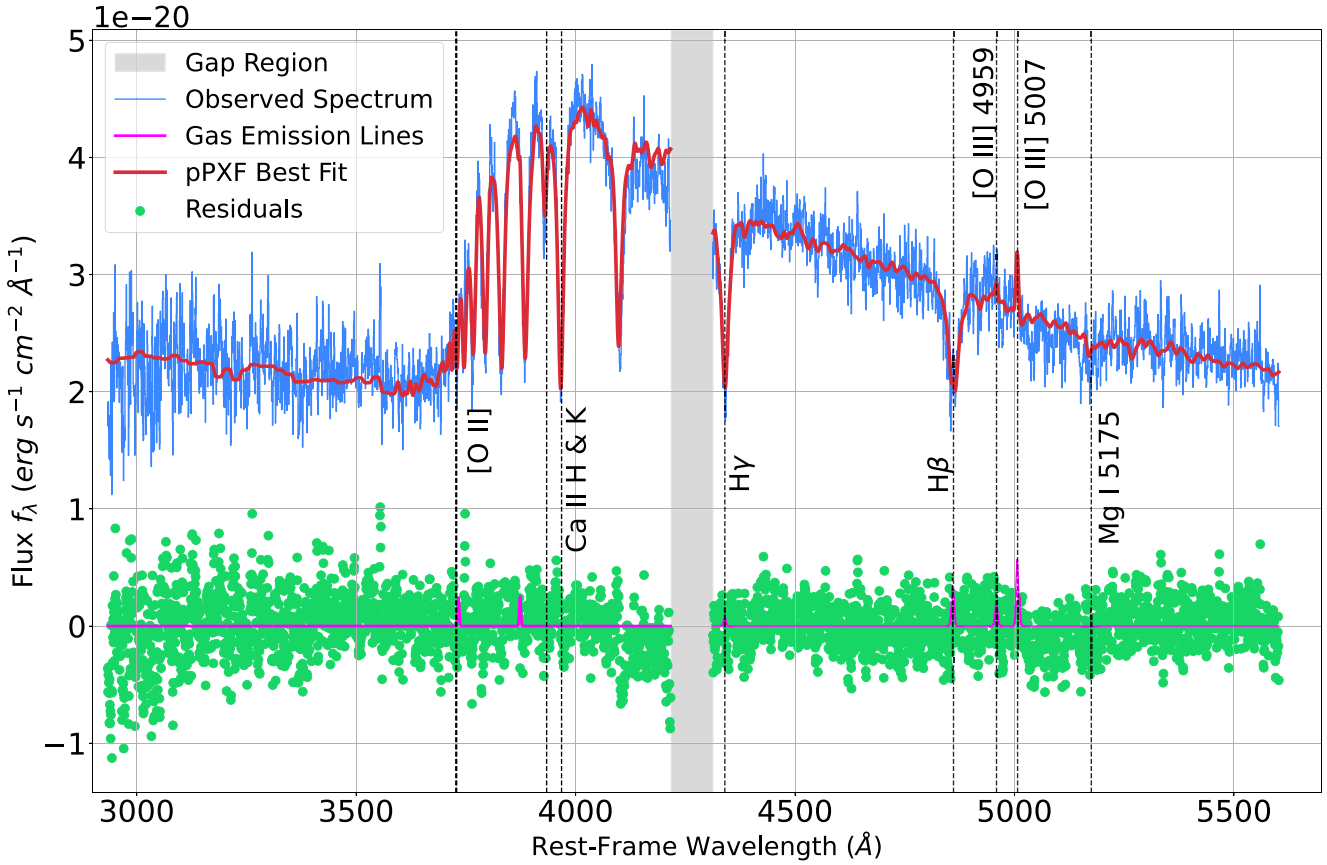

Figure 2. Spectrum of the galaxy GS-9209 in blue (within a 0.35 arcsec × 0.35 arcsec square aperture) smoothed and cleaned for outliers and non-valid values. It shows a strong Balmer break of ≈ 2–2.25, indicating that old stellar populations (spectral class A and later) dominate. Some particular absorption and emission lines are highlighted. We also show the spectrum fitted with the PPXF algorithm and the (weak) emission lines from the gas templates. The latter are shown overlaid on the residuals, which are displayed on the bottom of the figure.

and then extracts the sources based on a lower detection threshold value of 3 for the signal-to-noise ratio (S/N). The output of this procedure is a binary mask that can be used across multiple wavelengths from the data cube. We chose to make a combined mask that reunites the individual masks produced at the wavelengths corresponding to the NIRCam *F*200*W* filter (because we will do further photometric analyses in this bandpass) and to the [O III]λ5007 emission.

In our case, since we have an extended source, we use the function FIND_GALAXY from the MGEFIT package[2] (M. Cappellari 2002), which provides us with approximate values for the galaxy's centre position, ellipticity, and major axis. We are only interested in the major axis value because we select this as the size of the mask that we are using (7 spaxels = 0.35 arcsec). This is in agreement with the value where the light from the radial profiles of the galaxy becomes negligible.

2.1.2 *Background subtraction*

For the background subtraction, we use our own robust pipeline. First, the algorithm does a slice-by-slice background subtraction (these are wavelength slices) for each spaxel, using the function BACKGROUND2D from PHOTUTILS[3] (L. Bradley et al. 2024). Together with the areas of the galaxy itself (identified using the method described in Section 2.1.1), the spaxels with non-valid entries (NaN) are also masked for a given wavelength slice. We use MEDIANBACKGROUND from PHOTUTILS as a background estimator, together with a 3σ clipper (SIGMACLIP from ASTROPY; Astropy Collaboration 2022) that improves the robustness of the background level calculations and reduces the possibility of contamination from bright spaxels. There are also some wavelength slices for which this background subtraction procedure fails (often because of either excessive masking or due to issues with the slice itself e.g. being within the wavelength range of the detector gap). In these cases, our pipeline handles such slices by doing an interpolation based on neighbouring 'good' slices.

2.1.3 *Outliers removal*

We use the outlier-detection algorithm of F. D'Eugenio et al. (2024), but even after this step, some low-level artefacts remain. To remove them, we first mask any invalid values, then apply a median filter to smooth the spectrum, and clip any $> 3\sigma$ outliers. The resulting 'double-cleaned' spectrum is shown in Fig. 2, where

[2]Version 6.0.4, available at https://pypi.org/project/mgefit/

[3]We used version 2.0.1, but the most recent one is available at https://photutils.readthedocs.io/en/stable/

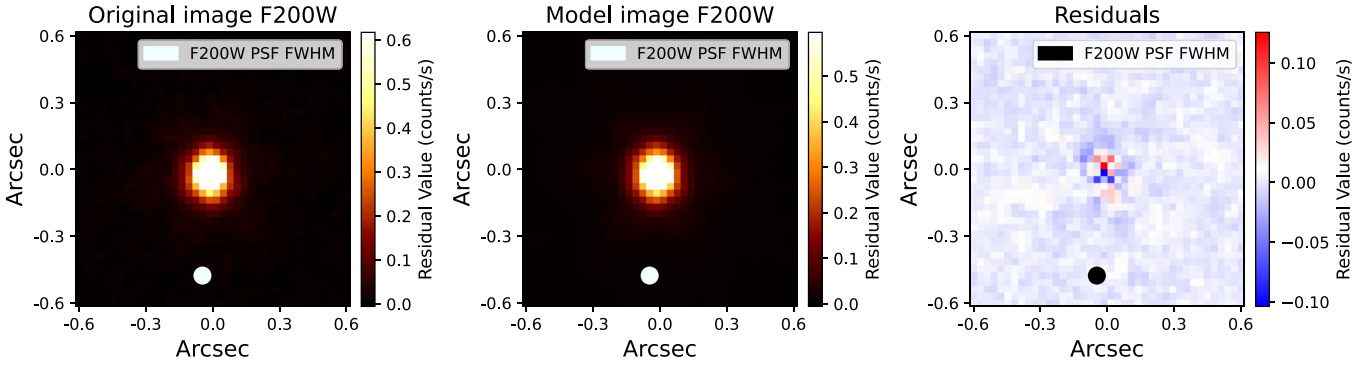

Figure 3. The original image in the NIRCam *F*200*W* band (a 40 × 40 pixels zoom-in around the brightest pixel; the NIRCam photometry pixel scale is 0.03 arcsec per pixel) is shown in the left panel. Results of the PySersic fitting procedure of the original image are displayed in the middle panel. The panel on the right-hand side illustrates the residuals from the fit i.e. res = original − model. On each of these images, we display the FWHM size (0.065 arcsec) of the PSF of the NIRCam instrument in the *F*200*W* band.

we extracted the spectrum from a 0.35 arcsec × 0.35 arcsec square aperture centred on the brightest spaxel of the cube median image. This image was obtained by taking the median flux value at each spaxel across all valid wavelength slices and spans approximately 5 $R_{\rm eff}$. The chosen aperture (illustrated in Fig. 1) is approximately the largest extent over which we can probe spatially resolved kinematics.

3 METHODS

3.1 Photometry analysis and morphology modelling

For kinematical calculations, we need an accurate model of the galaxy's surface brightness profile. Our approach requires Multi-Gaussian Expansion of the light profile (*MGE*; E. Emsellem, G. Monnet & R. Bacon 1994; M. Cappellari 2002). Since GS-9209 is highly compact (A. C. Carnall et al. 2023b), we follow the methods of J. Houdt et al. (2021); we first use a Sérsic model, taking advantage of its small number of free parameters (Section 3.1.1), and then re-parametrize this best-fitting model using *MGE* (Section 3.1.2).

3.1.1 Photometry modelling with PySersic

To determine our fiducial Sérsic profile, we used the PySersic[4] Bayesian fitting tool for galaxy photometry (I. Pasha & T. B. Miller 2023). We fit the galaxy image in the NIRCam *F*200*W* band and we use the empirical NIRCam ePSF from Z. Ji et al. (2024c) for this filter. The imaging data were obtained as part of JADES (*JWST* Advanced Deep Extragalactic Survey; D. J. Eisenstein et al. 2023), processed as described in M. J. Rieke et al. (2023), F. D'Eugenio et al. (2025), and D. J. Eisenstein et al. (2025). We show our results from PySersic fitting in Fig. 3; we will construct all our subsequent analysis based on the median values of the posterior distributions of the parameters of the model profile (given in Table 1).

In our analysis, we fit the background-subtracted NIRCam galaxy image to a Sérsic profile (J. L. Sersic 1968). The noise maps required as inputs for PySersic are taken from the background-removed photometry data. In order to evaluate the quality of the models, we have chosen the Student's *t* loss function, which is to be minimized by the fitting algorithm. For estimating the posterior distribution, we compare both the methods currently implemented into PySersic: Laplace method and SVI (stochastic variational inference) flow. The first method initially finds the Maximum A Posteriori (MAP) values of the parameters and assumes Gaussian posterior distributions around the MAP, whereas in the second (which we choose as fiducial), a normalized flow is trained to estimate the posterior distributions. We find that none of the results of our analysis depends on the method chosen; these results are consistent with each other, within their associated uncertainties (given in Tables 1 in the main text and A1 in Appendix A). The calculated effective radius is in agreement with the value obtained by A. C. Carnall et al. (2023b), but our Sérsic index 2.97 ± 0.14 is somewhat larger than the literature value (2.3 ± 0.3). For the next step, we used the median values of the posterior distributions from the PySersic fit – SVI method – in order to obtain the model image, de-convolved from the empirical PSF of the original *F*200*W* image. We also oversample by a factor of 10 with respect to the original image.

[4]version 0.1.5; https://github.com/pysersic/pysersic

Table 1. Best-fitting parameters for the PySersic *F*200*W* Image-SVI flow method. Here θ is the astronomical PA measured by PySersic from North (the *y*-axis) counterclockwise.

Parameter	Value
Observed ellipticity	0.251 ± 0.015
Sérsic index	2.97 ± 0.14
$R_{\rm eff}$ (arcsec)	0.0344 ± 0.0006
θ (deg)	173.9 ± 14.7

3.1.2 Multi-Gaussian expansion fitting of photometry

We perform a *MGE* fitting of the PSF de-convolved model image from PySersic. We used the MGE_FIT_1D procedure within the MgeFit package (M. Cappellari 2002). This procedure gives an approximation of the one-dimensional radial surface brightness profile (with a *MGE* re-parametrization) of the model image. Because the latter is, by construction, a purely Sérsic model, the surface brightness profile is given by (L. Ciotti & G. Bertin 1999):

$$I(R) = I_0 \cdot \exp\left[-b_n \cdot (R/R_{\rm eff})^{1/n}\right]. \quad (1)$$

In our case, since our procedure fits a normalized image ($L_{\rm tot} = 1$), we will need to convert to real physical units after doing the fit.

We can obtain I_0 using the equation (4) from L. Ciotti & G. Bertin (1999). In that equation, $b_n = 5.61$ for $n = 2.97$ (equation 18 from the same paper) and $\Gamma(2n) \approx 108.36$ for $n = 2.97$ (equation 7). With $R_{\rm eff} = 11.45$ pixels on the oversampled image, we get $I_0 = 0.106$ normalized arbitrary units per pixel[2].

Each Gaussian j has three parameters:

(i) The peak flux F_j given by the MGEFIT. This is measured in arbitrary units (relative to the normalized total luminosity) per pixel.

(ii) The dispersion of the two-dimensional Gaussian along the major axis, σ_j in pixels.

(iii) The observed axial ratio of the two-dimensional Gaussian, q'_j following the notation of M. Cappellari (2008). In the MGE_FIT_1D fitting procedure, this is not given as an output of the fit. We assume that all of the two-dimensional Gaussians have a fixed observed axial ratio $q'_j = 0.749$, the value given by the PYSERSIC photometry fitting tool.

GS-9209 has an apparent *F200W* band AB magnitude of $m_{\rm F200W} = 23.9$ mag. At the source redshift $z = 4.658$, this corresponds to an absolute magnitude $M_{\rm abs} = -22.38$ at a rest-frame wavelength $\lambda_{\rm rest} \approx 3510$Å. The pivot wavelength of the *F200W* bandpass is 19 875 Å and the absolute magnitude of the Sun in the *SDSS_u* bandpass (with a pivot wavelength of 3556 Å, close to the rest-frame wavelength that we are probing in the case of GS-9209) is $M_{u,\odot} = 6.39$ (C. N. A. Willmer 2018). This means that the absolute luminosity of GS-9209 (at rest-frame wavelength of ~ 3500 Å) is $L_{\rm gal,tot} = 3.4 \times 10^{11} L_\odot$. We then need to convert the integrated flux values that we have for our Gaussians, F_j to surface brightness values, which we will use in our Jeans anisotropic modelling (JAM) algorithm. This is done using the following equation (M. Cappellari 2002, 2008):

$$I_j = \frac{F_j}{\sigma_j \sqrt{2\pi}}. \quad (2)$$

3.2 Spectrum fitting with PPXF

To measure the stellar kinematics, we use the PPXF[5] software, an efficient full spectral fitting algorithm (M. Cappellari & E. Emsellem 2004; M. Cappellari 2017, 2023). PPXF is able to simultaneously fit both the stellar continuum and gas emission lines so one can extract the kinematics of multiple components (e.g. F. Belfiore et al. 2019; K. B. Westfall et al. 2019). The algorithm constructs a model of the galaxy as a linear combination of individual spectral templates, convolved with the line-of-sight velocity distribution (LOSVD).

In our work, we used templates built using FSPS v 3.2 (C. Conroy & others 2009; C. Conroy & J. E. Gunn 2010), with the *MILES* stellar library for the optical region (P. Sánchez-Blázquez & others 2006; J. Falcón-Barroso & others 2011) and with the *MIST* isochrones (J. Choi et al. 2016). We adopted a E. E. Salpeter (1955) initial mass function (IMF), but this choice has no impact on the derived stellar kinematics. This is because for the stellar-population age of the target (~ 500 Myr; A. C. Carnall et al. 2023b) and spectral range of our data we do not track a wide enough variety of IMF-sensitive features. In order to determine the IMF characterizing GS-9209, we need to use the M_*/L ratio result from the *JAM* dynamical modelling (Section 4.2).

The stellar spectral templates have an instrumental resolution with constant full width at half-maximum (FWHM) $\Delta\lambda_{\rm temp} \approx 2.5$ Å (J. Falcón-Barroso et al. 2011). For comparison, the average rest-frame instrumental resolution that we have for the galaxy spectra observations is $\Delta\lambda_{\rm instr} \sim 1.5$Å $= \langle\lambda\rangle / \langle R\rangle$ with $\langle\lambda\rangle = \sqrt{\lambda_{\rm min,rest} \cdot \lambda_{\rm max,rest}}$ and $\langle R\rangle \sim 2700$. Since the resolution of the data is better than the resolution of the templates, we need to correct the derived stellar dispersion using the following equation (adapted from equation 5 from M. Cappellari 2017):

$$\sigma_*'^2 = \sigma^2_{*,\rm ppxf} - \sigma^2_{\rm instr} + \sigma^2_{\rm templ}, \quad (3)$$

where $\sigma_{*,\rm ppxf}$, the velocity dispersion indicated by the PPXF algorithm, is not the same as the intrinsic (but not de-projected yet) velocity dispersion, σ'_*. We need to correct for the Gaussian dispersions of the line spread functions of the instrument observing the galaxy ($\sigma_{\rm instr}$) and of the stellar templates that we used in our analysis ($\sigma_{\rm templ}$). In order to convert from $\Delta\lambda_{\rm templ}$ to $\sigma_{\rm templ}$ or from $\Delta\lambda_{\rm instr}$ to $\sigma_{\rm instr}$ we use the general formula (valid for both cases):

$$\sigma_{\rm j} = \frac{c \cdot \Delta\lambda_{\rm j} \lambda_{\rm med}}{2.355}, \quad (4)$$

where 'j' = either 'templ' or 'instr' and $\lambda_{\rm med}$ is the median wavelength of our range. To confirm the accuracy of our methods, we repeated our analysis by using stellar templates from a higher resolution library[6] ($R \sim 3200$), which uses the *C3K* model atmospheres (C. Conroy et al. 2019) instead of *MILES*. The results did not differ by more than a few per cent compared to our original method (e.g. for the spectrum in Fig. 2 using *MILES* stellar spectra, we obtained $\sigma'_* = 239 \pm 34 {\rm km\,s^{-1}}$ compared to $234 \pm 37 {\rm km\,s^{-1}}$ when using *C3K*). This is in good agreement with the value obtained by A. C. Carnall et al. (2023b, using medium-resolution spectroscopy) for the stellar dispersion $\sigma'_* = 247 \pm 16 {\rm km\,s^{-1}}$.

3.3 Voronoi bins analysis

The purpose of the Voronoi binning algorithm is to perform a two-dimensional re-binning of our spectral data to achieve a minimum S/N threshold. We create S/N maps for all the spaxels using the median-filtered signal across the wavelength slices for which $\lambda_{\rm rest} < 3500$ Å. As can be seen from Fig. 2 this represents the flattest region of the spectrum, so the computed S/N is not affected too much by the presence of absorption/emission lines or by the slope of the continuum. We mask all the noise dominated spaxels with S/N < 1. We used the VORBIN[7] package (M. Cappellari & Y. Copin 2003). We set a threshold S/N target > 3 for our Voronoi bins.

For each Voronoi bin, we obtain the spectrum as the sum of the spectra of the pixels contained within that bin. The spectrum for each Voronoi bin has been further processed as follows:

(i) In the case of each spectrum, the non-valid values and the $> 3\sigma$ outliers were masked. This creates the 'cleaned' Voronoi bin spectrum, which is then smoothed using a median filter. The smoothed spectrum is not brought forward into our analysis but it is used only to identify and mask bad spectral pixels.

[5]We used version 9.4.1; the software is available from https://pypi.org/project/ppxf/

[6]These templates are available from the authors C. Conroy upon reasonable request.

[7]We used version 3.1.5, available from https://pypi.org/project/vorbin/

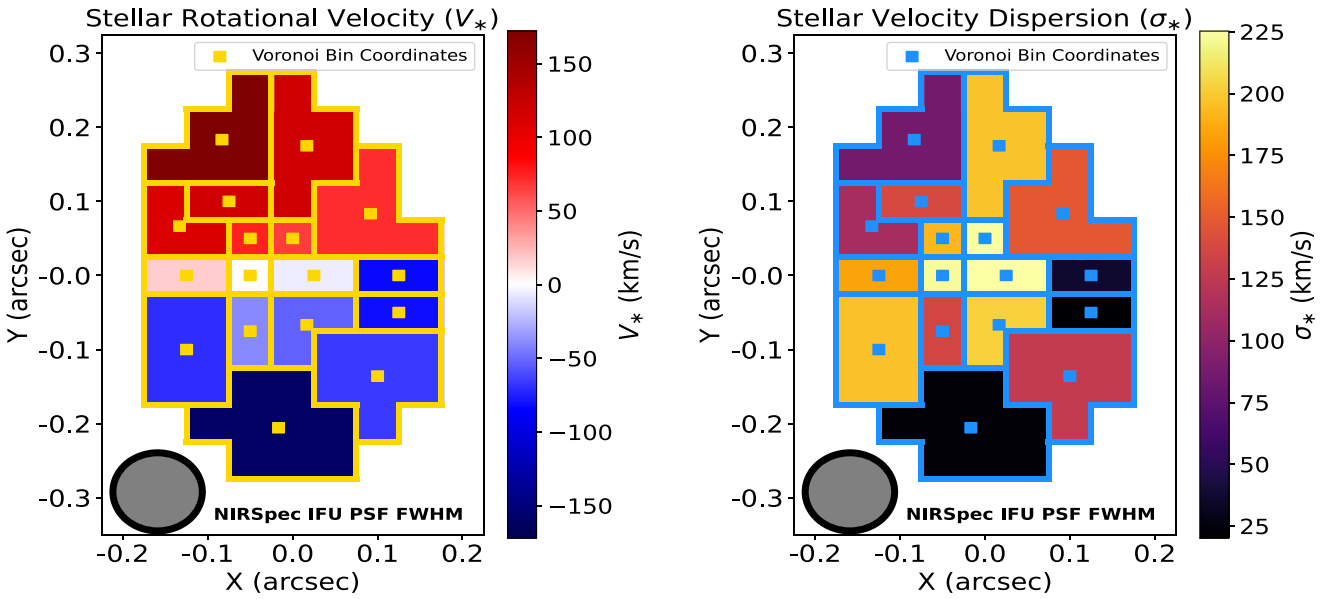

Figure 4. Maps of the observed (i.e. not de-projected) first (left panel) and second (right panel) moments of the stellar kinematics for the MQG GS-9209 i.e. the stellar line-of-sight velocity (V_*) and the stellar velocity dispersion (σ_*). The left panel indicates a rotational pattern of the motions of the stars in this galaxy. The right panel shows a dispersion-dominated central region. The spatially resolved kinematics maps extend to about 4 spaxels = 0.2 arcsec, which means approximately 6 $R_{\rm eff} \approx 1.3$ kpc. We furthermore show the outlines separating the Voronoi bins from each other and the positions of the centres of each Voronoi bin. The spaxels contained within each Voronoi bin are all colour coded according to either V_* (left panel) or σ_* (right panel). The plots also display the PSF FWHM of the NIRSpec IFU instrument at $\lambda_{\rm obs} = 2$ μm.

(ii) We log-rebin each 'cleaned' spectrum to a velocity scale $c \times \ln(\lambda_{\rm max}/\lambda_{\rm min})/N_\lambda \approx 50$ km s^{-1} (here N_λ represents the number of wavelength slices) and run an initial PPXF fit. We impose constraints on the ages and metallicities ranges of the templates to be used: age < 1.3 Gyr (the age of the Universe at $z \sim 4.66$) and $-1 \leq \log(Z/Z_\odot) \leq 0.5$. The purpose of allowing high-metallicity templates is to capture the effect of α-elements enrichment (e.g. A. G. Beverage et al. 2021, 2023; A. C. Carnall et al. 2024). The goal of this initial PPXF run on the cleaned spectra is to reduce the numbers of stellar templates that we use. We determine the stellar templates (in this first run of the PPXF fit) for which the light weights are positive. These stellar templates will be used in the second fit (the gas templates remain unchanged).

(iii) We then run a second PPXF fit on the 'cleaned' Voronoi bin spectra and the results of this fit are used for further analysis, specifically the stellar kinematic values $V_{*,\rm ppxf}$, the stellar rotational velocity, and $\sigma_{*,\rm ppxf}$, the stellar velocity dispersion returned by PPXF, together with the uncertainties in each of these parameters. We use equation (3) in order to take into account the difference between the stellar velocity dispersion returned by PPXF and the value corrected for instrument and templates line widths.

Using the intrinsic velocity dispersion (obtained after applying the correction from equation (3)) we build our $V_{\rm rms}$ map that is required for our subsequent *JAM* Dynamical Modelling (Section 4.2). Here $V_{\rm rms} = \sqrt{V_*^2 + \sigma_*^2}$.

4 RESULTS

4.1 Spatially resolved kinematics maps of GS-9209

The results of our stellar kinematics analysis are shown in Fig. 4. The image on the left side shows that the stars in this galaxy have substantial angular momentum around the galaxy centre. The image on the right side shows a decrease of the stellar velocity dispersion from the galaxy centre to its outskirts. With our kinematics data alone, it is difficult to disentangle between beam smearing effects and the plausible explanation of this structure being related to the presence of a dispersion-dominated central bulge. This information can be revealed if we combine spatially resolved kinematics data and resolved stellar population ages maps. The key point of this analysis is that the disc-like kinematics is still preserved after the quenching took place. Hence, it turns out that galaxies may first stop forming stars (and quench inside-out) but preserve their disc-like kinematics for another time interval before other dynamical processes may come into play and transform them into the slowly rotating spheroids and early-type galaxies (ETGs) that we observe at $z \sim 0$.

4.2 JAM dynamical modelling

JAM is a robust method that is suitable for a plethora of galaxies dynamical modelling tasks including estimating the galaxies dark matter content (G. de Ven et al. 2010; M. Barnabè et al. 2012; S. Comerón et al. 2023), computing central SMBHs (D. A. Drehmer et al. 2015; A. Feldmeier-Krause et al. 2017; S. Comerón et al. 2023) or determining dynamical masses to high accuracy (R. P. Marel & P. G. Dokkum 2007; M. Cappellari et al. 2009; J. Houdt et al. 2021; M. Cappellari 2023; K. Zhu et al. 2023). The better performance and accuracy of *JAM* has been tested and acknowledged against other techniques such as the more generalized Schwarzschild dynamical models (M. Schwarzschild 1979). Such tests were done using either simulated data (Y. Jin et al. 2019) or real data (G. Y. C. Leung et al. 2018). These tests revealed the ability of this method to accurately produce a robust dynamical

model for a wide variety of input kinematics data. In our study, we use the JAMPY package.[8]

To calculate the posterior probability distributions on the model parameters, we use the Adaptive Metropolis algorithm (N. Metropolis et al. 1953) as implemented within the ADAMET package[9] (M. Cappellari et al. 2013a). We repeated our analysis using the Markov Chain Monte Carlo sampling alogirthm EMCEE (J. Goodman & J. Weare 2010; D. Foreman-Mackey et al. 2013) and we concluded the results obtained were statistically consistent but that ADAMET algorithm had a better time efficiency by a factor of ~ 2.

Our *JAM* dynamical models rely on the assumption that our galaxy is axisymmetric and furthermore that there is no spatial variation of the M_*/L ratio or of the radial anisotropy parameter (P.-Y. Lablanche et al. 2012). This assumption is motivated by the findings of K. A. Suess et al. (2021) who report that massive PSB galaxies at $2 < z < 2.5$ typically have flat colour gradients. The outputs from the *MGE* fitting of the *F*200*W* photometry (surface brightness, dispersions along the major axis and observed axial ratios of the Gaussians) are given as inputs for the light map of *JAM*. The choice of *F*200*W* band to construct these flux maps is justified because in this way, we capture the stellar light at rest-frame wavelengths near the Balmer break ($\lambda_{\rm rest} \sim$ 3500-4000 Å) primarily coming from type A-stars dominating the spectrum of GS-9209. Furthermore, at these wavelengths, we avoid possible contamination from faint AGNs that might be present at lower rest-frame wavelengths.

The coordinates of the Voronoi bins that we pass on to *JAM* were rotated such that the major axis of the galaxy is parallel to the horizontal axis of the new coordinate system. This means that we need to rotate our $x_{\rm bin}$ and $y_{\rm bin}$ counterclockwise by an angle of -98° (the best-fitting position angle retrieved by the PAFIT algorithm[10]). This value agrees to within 2° with the negative of the position angle measured clockwise from the image *x*-axis. i.e. $270^\circ - \theta$, where θ is the astronomical PA measured by PYSERSIC from North (the *y*-axis) counterclockwise, suggesting a very good alignment of the kinematic axis to the morphological major axis. Our *JAM* dynamical modelling algorithm further requires the size of the PSF as an additional input. We assume a two-dimensional Gaussian PSF of circular shape i.e. with the same FWHM in both the direction of the NIRSpec/IFU slicers and perpendicular to them. The NIRSpec PSF size that we give as an input to *JAM* is the geometrical average between the values given by the equations (3) and (4) from F. D'Eugenio et al. (2024) adopting a typical wavelength of $\lambda \sim 2$ μm (because our photometry analysis was based on NIRCam *F*200*W* data). In our case, this average value is $\mathrm{FWHM_{PSF}} = 0.104$ arcsec.

All the dynamical models that we build assume a cylindrically aligned framework of the velocity ellipsoid (M. Cappellari 2008). Our fiducial dynamical model assumes a Navarro–Frenk–White (NFW; J. F. Navarro, C. S. Frenk & S. D. M. White 1996) density profile for the dark matter halo and a Gaussian probability prior on the logarithm of the central BH mass (with the mean being $\langle \log \mathrm{M_{BH}}/\mathrm{M_\odot} \rangle = 8.8$ and a standard deviation of 0.3). The choice for the mean and the standard deviation of this Gaussian prior is motivated by the results from the broad-line component of H α fit obtained by A. C. Carnall et al. (2023b). The reason for imposing a prior on the central BH mass is because our spatial resolution of 0.05 arcsec spaxel^{-1} is about 6.5 times larger than the radius of the black hole's sphere of influence (assuming the mass obtained by A. C. Carnall et al. 2023b). This is discussed in Appendix B and illustrated in Fig. B1 where we present our *Alternative-1* Black-Hole-Mass-Follows-Light (BH + MFL) model used to infer the central BH mass, which was allowed to be fit freely by the *JAM* algorithm. The other parameters of *Alternative-1* the dynamical model (reported in Table B1) agree within 1σ uncertainties with the values obtained from our *Fiducial* dynamical model (the latter were reported in Table 2).

Table 2. Marginalized posterior probabilities on the free parameters of our fiducial dynamical model (which assumes an NFW Dark Matter density profile and a Gaussian prior on $\log M_{\rm BH}$; see the main text). The values reported are the median and 16th–84th percentile probability range.

Parameter	Value	Model
$q_{\rm intr}$	0.62 ± 0.10	*Fiducial*
σ_z/σ_R	0.85 ± 0.08	*Fiducial*
$\log f_{\rm DM}\,(< 2R_{\rm eff})$	-0.84 ± 0.15	*Fiducial*
$\log\left[(M_*/L)\,/\,(\mathrm{M_\odot}/L_\odot)\right]$	-1.01 ± 0.06	*Fiducial*
$\log M_{\rm BH}/\mathrm{M_\odot}$	imposed prior	*Fiducial*

We obtain a stellar mass for this galaxy of $\log(\mathrm{M_*/M_\odot}) = 10.52 \pm 0.06$ from our *Fiducial* dynamical model. This value is consistent within 1σ with the value of 10.58 ± 0.02 estimated by A. C. Carnall et al. (2023b) from stellar population modelling. In any case, we can see from e.g. fig. 1 of Q. Duan et al. (2024) that this galaxy is at least 3σ more massive than the median of the redshift range $4.5 \leq z \leq 6.5$.

In our fiducial dynamical model, the dark matter density profile is assumed to be classical NFW (with the small radius slope $\gamma = -1$) satisfying the equation (J. F. Navarro et al. 1996; J. S. B. Wyithe, E. L. Turner & D. N. Spergel 2001):

$$\rho_{\rm DM}(\mathrm{r}) \propto \frac{1}{(\mathrm{r/r_b})^{-\gamma} \cdot (1 + \mathrm{r/r_b})^{\,3+\gamma}}, \tag{5}$$

$\mathrm{r_b}$ is the break radius of the dark matter (DM) Halo in which GS-9209 resides. Using the stellar mass–halo mass relation results from the fig. 7 of P. S. Behroozi, R. H. Wechsler & C. Conroy (2013), we deduce that the halo of GS-9209 has a mass of $\log(\mathrm{M_h/M_\odot}) \approx 12.36 \pm 0.10$. Then we determine the virial radius of our DM Halo, $R_{\rm vir}$, from

$$\mathrm{M_h} = \frac{4\pi}{3} \Delta_{\rm vir} \rho_{\rm m}(\mathrm{z})\, \mathrm{R_{vir}^3}. \tag{6}$$

In this equation, we assume that the density contrast is $\Delta_{\rm vir} = 200$. Doing the calculation we obtain $R_{\rm vir} \approx 70 \pm 6$ kpc. Next, we estimate the concentration parameter $\mathrm{c_{200}} = \mathrm{R_{vir}/r_b}$ from Fig. 5 of A. A. Klypin, S. Trujillo-Gomez & J. Primack (2011). We obtain a value of $c_{200} = 4.7 \pm 0.2$, which gives $r_b = 14.9 \pm 1.4$ kpc. This is the reason for which we have chosen to fix this break radius in our calculations to 15 kpc (2.31 arcsec at this redshift) in our *JAM* dynamical modelling algorithm. In a similar way to the method illustrated in Section 3.1.2, we fit this NFW profile to obtain the *MGE* Gaussians for the Dark Matter component. Subsequently, the one-dimensional *MGE* best fit of the dark matter halo density profile and the *MGE* fit of the stellar component light profile (constructed in Section 3.1.2) are combined.

The dynamical model is used to determine a number of parameters that define either the morphology or the structure of this galaxy:

[8] version 8.0.0, available at https://pypi.org/project/jampy
[9] version 2.0.9 available from https://pypi.org/project/adamet/
[10] version 2.0.8 available from https://pypi.org/project/pafit/

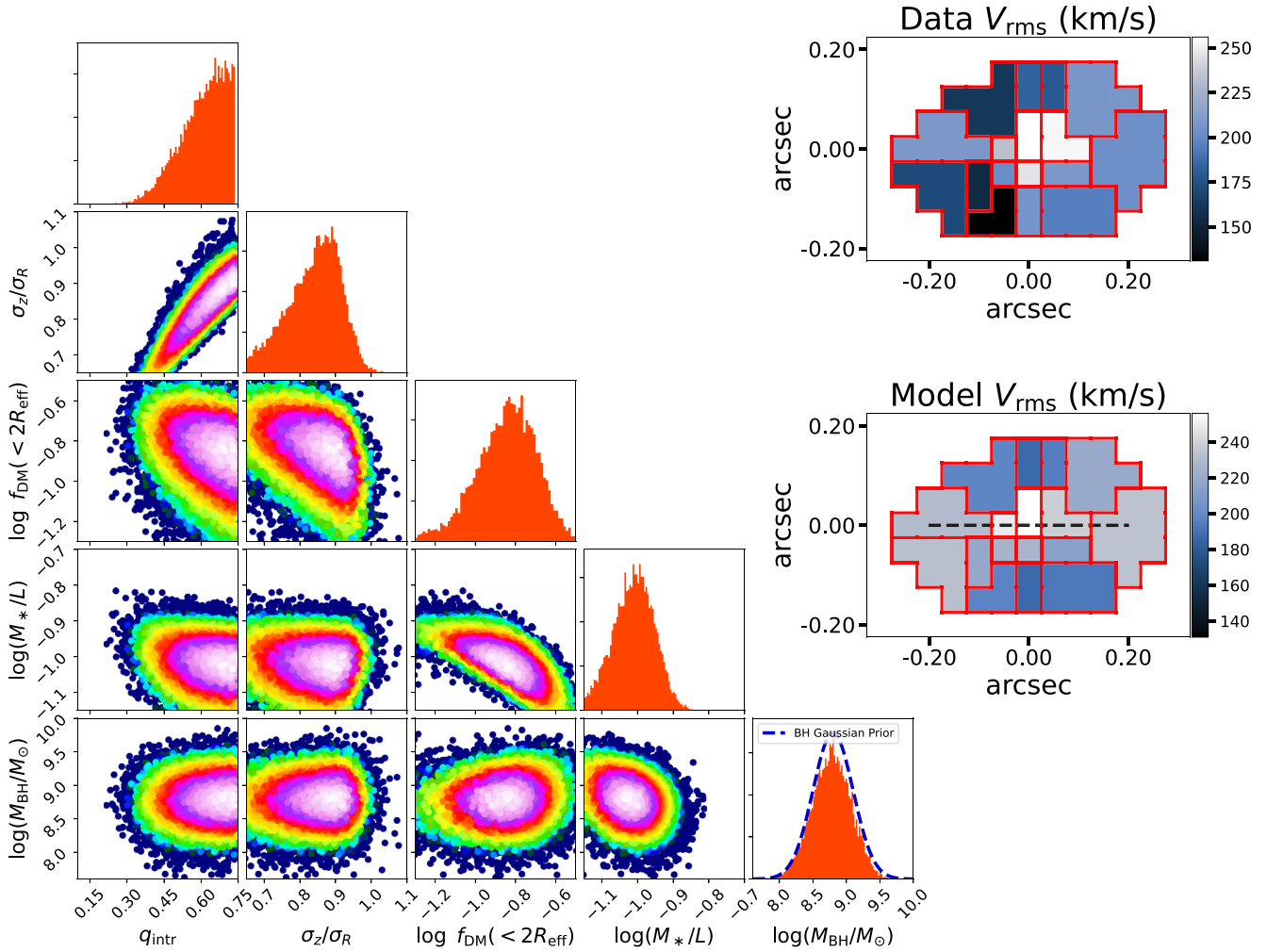

Figure 5. Outputs of the fiducial dynamical model. In this model, we consider a Gaussian prior on the mass of the central BH (as shown on the bottom right corner plot panel; see the details in Section 4.2) and we furthermore assume a classic NFW density profile of the dark matter halo. We obtain a Dark Matter fraction of about $14.5^{+6.0}_{-4.2}$per cent within two effective radii. In this plot, we denote $\log(M_*/L) \equiv \log[(M_*/L)\,/\,(\mathrm{M}_\odot/L_\odot)]$. The fiducial dynamical model has $\chi^2_r = 1.4$. The central black dashed line corresponds to the major axis of the galaxy, which we will use in the calculation of $(V/\sigma)_*$ in Section 4.4.2.

(i) $\mathbf{q}_{\rm intr}$, the intrinsic axial ratio. Combined with the observed axial ratio, this will give us the inclination angle of the galaxy with respect to the line of sight. The latter is crucial in computing the de-projected values of various kinematic parameters (Section 4.4).

(ii) $\boldsymbol{\sigma_z}$ $\boldsymbol{\sigma_R}$, the radial anisotropy of the velocity ellipsoid (cylindrically aligned). This is also used in de-projection calculations.

(iii) $\mathbf{M}_*/\mathbf{L}$, the stellar mass to light ratio.

Because $V_{\rm rms}$ is independent of the tangential anisotropy (see the discussion in section 3.1.5 of M. Cappellari 2008), we need to test another dynamical model *Alternative-2* in order to determine the tangential anisotropy $\sigma_\phi/\sigma_{\rm R}$ (this parameter is required for subsequent de-projection calculations). We fit the first-order velocity moment along the line of sight i.e. the V_* spatially resolved map from the left panel of Fig. 4 with the *JAM* keyword input *moment* = *'z'*. In this model, we again assume a classic NFW DM halo density profile and Gaussian priors on each of the parameters $q_{\rm intr}$, $\sigma_{\rm z}/\sigma_{\rm R}$, $\log f_{\rm DM}\,(<2R_{\rm eff})$, $\log[(M_*/L)\,/\,(\mathrm{M}_\odot/L_\odot)]$, and $\log(M_{\rm BH}/\mathrm{M}_\odot)$. The means and the standard deviations of their Gaussian priors are taken as the best fit and the uncertainty estimates produced as outputs of *Fiducial* dynamical model (Table 2). We introduce the new parameter $\sigma_\phi/\sigma_{\rm R}$ to be fitted by the *JAM* algorithm. We impose an informative Gaussian prior on this parameter with a mean of 1 and a standard deviation of 0.2 as motivated by the second panel of fig. 2 from M. Cappellari et al. (2007). The outcome posterior distributions of this model are shown in Fig. C1 in Appendix C, with the mean and the uncertainties given by the 16$^{\rm th}$ and 84$^{\rm th}$ percentiles reported in Table C1. We are thus able to put a tight constraint $\sigma_\phi/\sigma_{\rm R} = 1.01 \pm 0.05$.

4.3 Dynamical mass of GS-9209

We compute the total dynamical mass of this galaxy using equation (7) from A. der Wel et al. (2022) (assuming that our galaxy behaves kinematically similar to a disc; this is justified by the rotation pattern that we can see in spatially resolved V_* map; Fig. 4):

$$\mathrm{M_{dyn}} = \mathrm{K}\,(\mathrm{n_{ser}})\,\mathrm{K}\,(\mathrm{q'})\,\mathrm{R_{eff}}\sigma'^2_*/\mathrm{G}. \quad (7)$$

We use the same parametrizations as in A. der Wel et al. (2022); this parametrization assumes that the total dynamical mass is two times larger than the mass predicted by *JAM* dynamical modelling within the half light radius: $M_{dyn} = 2 \times M_{JAM} (< R_{eff})$. In this equation, $K(n_{ser})$ is given by eq. (20) of M. Cappellari et al. (2006). This correction factor depends on the Sérsic index (we adopt a value $n_{ser} = 2.97 \pm 0.14$ following the results of the PySERSIC photometric fitting and given in Table 1), whereas $K(q')$ depends on the observed axial ratio, for which we take $q' = 1 - \epsilon' = 0.748 \pm 0.015$ with ϵ' also taken from the PySERSIC fitting results (Table 1). From the PySERSIC photometry fitting, we have that $R_{eff} = 223 \pm 4$ pc. This uncertainty is propagated from the PySERSIC fitting and is not our actual error for R_{eff}. We estimate the latter to be around ± 20 pc, taking into account the systematic uncertainties. For the stellar velocity dispersion, we take σ'_* to be the non de-projected value that we obtained from the PPXF full spectrum fitting i.e. $\sigma'_* = 239 \pm 34\,\mathrm{km\,s^{-1}}$ (Section 3.2).

Using these values, we obtain $\log(M_{dyn}/M_\odot) = 10.3 \pm 0.3$. The quoted uncertainties are dominated by systematics such as the calibration uncertainty of the virial estimator scaling relation. Overall, this result is consistent (within the 1σ uncertainties) with the stellar masses that we have found using our *Fiducial* dynamical model ($\log(M_*/M_\odot) = 10.52$). A considerably more robust method of computing the dynamical mass was proposed in section 5.2 of M. Cappellari (2023) and relies on the use of JAM_AXI_SERSIC_MASS procedure, which has a number of important advantages such as allowing us to pass as inputs the size of the PSF and our custom rectangular aperture (0.35 arcsec × 0.35 arcsec) that we used to produce the spectrum in Fig. 2. Furthermore, the method takes into account the effects of inclination and radial anisotropy when predicting the dynamical mass of the Sérsic model of our galaxy. With $n_{Ser} = 2.97$, and the values for R_{eff} and σ'_* mentioned above, we obtain a remarkably similar value: $\log(M_{dyn,JAM}/M_\odot) = 10.32 \pm 0.14$. Our result is consistent with the fact the target has a relatively low dark matter fraction, as inferred from our fiducial dynamical model (Fig. 5), with the total density of this galaxy being close to its stellar density.

4.4 Quantitative analysis of the galaxy's kinematics

To allow for a better comparison with the observationally retrieved kinematics parameters of other galaxy samples from the literature or with the characteristics of galaxies in numerical simulations, we must compute some quantities that numerically quantify the rotational pattern observed in this galaxy and the net contribution of rotation itself to the total kinetic energy budget of the galaxy. These are:

(i) $\boldsymbol{(V/\sigma)_*}$ the ratio of between stellar rotational velocity and velocity dispersion.

(ii) $\boldsymbol{\lambda_{2R_{eff}}}$: the spin parameter of our galaxy, calculated using all the bins available within a projected distance of $\leq 2\,R_{eff}$ from the galaxy's centre. The reason for choosing an aperture of $2\,R_{eff}$ instead of the conventional $1\,R_{eff}$ is because of the fact that we only have one Voronoi bin within the latter aperture. We adopt the effective radius and the galaxy's centre position that were determined by PySERSIC.

(iii) $\boldsymbol{\kappa_{rot}} = (\mathrm{K.E.})_{rot} / (\mathrm{K.E.})_{total}$. This is the fraction of kinetic energy that goes into ordered stellar rotation (defined in the same way as in L. V. Sales et al. 2012).

4.4.1 *Inclination angle; de-projection calculations*

The intrinsic (de-projected) axial ratio of the galaxy, q_{intr}, is a free parameter that our *JAM* algorithm provides a best fit for. In the *Fiducial* model (which is more robust compared to the BH-MFL one in Appendix B), *JAM* predicts a value $q_{intr} = 0.62 \pm 0.10$ (Table 2), although the data do not provide tight constraints, since the posterior probability distribution is consistent with the upper limit set by the priors (Fig. 5). In order to test the robustness of this estimate, we conduct a further dynamical model test *Alternative-3*. In this model, we use the same set-up as in the *Fiducial* model but this time we put an additional Gaussian prior on q_{intr} with a mean of 0.41 and a standard deviation of 0.18. The choice for these values is motivated by the study of J. Houdt et al. (2021) on a sample of massive galaxies from the LEGA-C survey (A. Wel et al. 2016). While these values apply to a sample of galaxies at $0.6 < z < 1$, there are currently no similarly large spectroscopic surveys of quiescent galaxies at much higher redshifts than this LEGA-C sample. As given in Table D1 the *Alternative-3* dynamical model gives $q_{intr,3} = 0.58 \pm 0.09$ and it has a higher reduced χ^2_r than the *Fiducial* dynamical model. Since $q_{intr,3}$ is significantly closer to q_{intr} retrieved by the fiducial model than to the mean of the prior imposed on this parameter within the *Alternative-3* dynamical model, it means that we can trust the reliability of our data to determine the true value of the intrinsic axial ratio of GS-9209. Hence, we assume $q_{intr} = 0.62$ in our subsequent calculations. This value agrees with the median axial ratio found by L. Kawinwanichakij et al. (2025) for a sample of 17 MQGs at $3 < z < 4.3$ (originally from T. Nanayakkara et al. 2025).

The equation that relates the observed axial ratio, the intrinsic axial ratio, and the inclination of our line of sight compared to the galaxy axis of symmetry is the equation (14) from M. Cappellari (2008). Rearranging the terms, we have

$$\tan i = \sqrt{\frac{1 - q'^2}{q'^2 - q^2_{intr}}}. \tag{8}$$

We obtain an inclination angle of $i = 57.8^\circ \pm 9.5^\circ$ ($i = 0^\circ$ would correspond to a face-on view). The inclination angle that we obtain for GS-9209 is surprisingly (although not physically impossibly) high. We should keep in mind the fact that this galaxy exhibits line emission from the AGN broad-line region (BLR; A. C. Carnall et al. 2023b). There have been several studies about BLRs, Type-1 AGNs, and Seyfert-1 galaxies from a geometrical perspective (T.-Z. Zhang & X.-B. Wu 2002; R. Decarli, M. Dotti & A. Treves 2011; L. Kuhn et al. 2024). The general consensus is that the maximum half-opening angle of the cone of BLR emission is somewhere in the region $\theta_o \approx 50^\circ$-$60^\circ$, which means that, in our case, the detection of broad-line H α emission in GS-9209 implies that the inclination angle should (conservatively) be below 60°. Given the inclination angle value of $i \approx 58^\circ$ for GS-9209, it means that the line of sight is only barely inside the BLR emission cone. Although the distribution of the inclination angles for general BLRs is peaked at around $\langle i \rangle \approx 30^\circ$ if we assume thin disc shapes (R. Decarli et al. 2011), there have been studies that reported an inclination angle close to the cone half-opening angle and also close to about 60° (e.g. M. C. Bentz, P. R. Williams & T. Treu 2022). In other cases, the inclination angles of the galactic disc and the inclination angle of the BLR are widely different but broad-line emission is still detected (e.g. sources MCG+04-22-042, Mrk 1392 or Zw 229 − 015; R. Du et al. 2025).

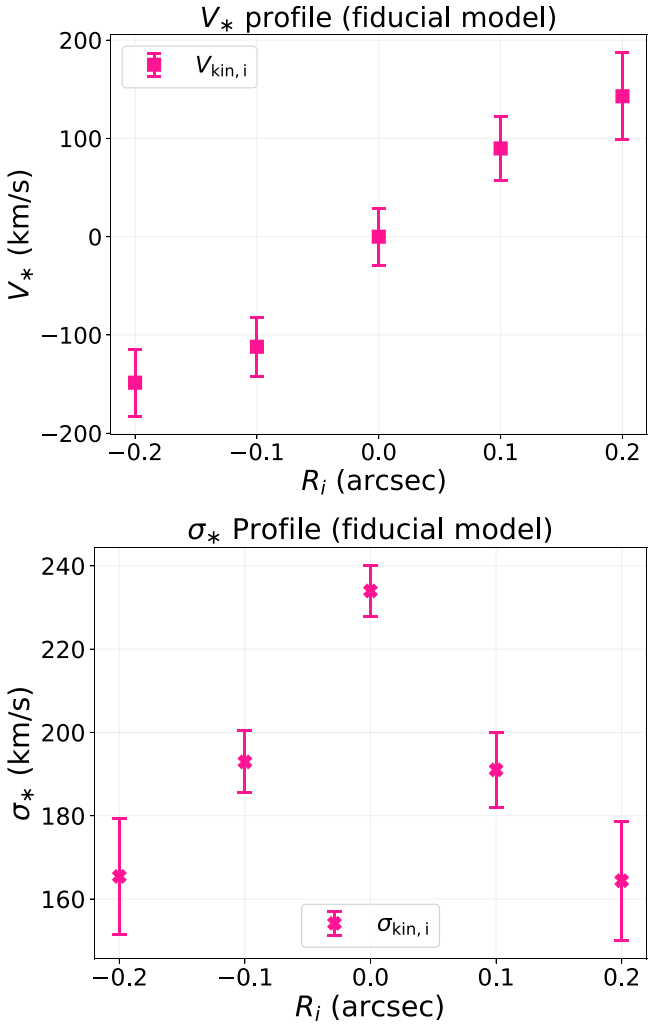

Figure 6. Non-deprojected stellar kinematics first and second moments (V_*– top panel and σ_*– bottom panel, together with their 1σ uncertainties) radial profiles obtained from the fiducial dynamical model.

4.4.2 V/σ

We adopt the following method for determining $(V/\sigma)_*$. We consider a set of points located on the major axis of the galaxy (in the rotated coordinate system in which the major axis is in the horizontal direction). Therefore, we select this set of points in the projected space such that they have $y_{\rm rot,P} = 0$ and they are equally spaced between $x_{\rm rot,P} = -4$ spaxels and $x_{\rm rot,P} = +4$ spaxels along the major axis indicated on the bottom panel on the right-hand side of Fig. 5 (4 spaxels mean 0.20 arcsec, which is approximately the size of the region we can extract kinematics data from). For each Voronoi bin 'V' (located at coordinates $x_{V,k}$ and $y_{V,k}$ with $0 \leq k \leq 16$) we compute the angular distances to each point 'P' on galaxy's major axis ($x_{p,i}$ and $y_{p,i} = 0$ for $0 \leq i \leq 4$; we chose to sample the data points at distances of 0.1 arcsec from one another, giving a total of five points on the galaxy's major axis): $d_{i,k} = \sqrt{y_{V,k}^2 + \left(x_{V,k} - x_{p,i}\right)^2}$. Then for each constructed point on the galaxy's major axis we define a kinematic rotational velocity $V_{\rm kin,i}$ and velocity dispersion $\sigma_{kin,i}$ such that

$$V_{\rm kin,i} = \left(\sum_{k=0}^{16} V_k/d_{i,k}^2\right) \Big/ \left(\sum_{k=0}^{16} 1/d_{i,k}^2\right), \tag{9}$$

$$\sigma_{\rm kin,i} = \left(\sum_{k=0}^{16} \sigma_k/d_{i,k}^2\right) \Big/ \left(\sum_{k=0}^{16} 1/d_{i,k}^2\right). \tag{10}$$

V_k and σ_k are the rotational velocity and the velocity dispersion (for the Voronoi bin 'k') computed by our *Fiducial* dynamical model for the Voronoi bin 'k'. In this section, V_k and σ_k can be regarded as the PSF-deconvolved kinematics map values obtained within the *Fiducial* dynamical model (Fig. 6). These are retrieved by setting the keywords in *JAM*: ANALYTIC_LOS = *False* and INTERP = *False*.

Using the equations (9) and 10, we obtain the radial profile data points (the pink cross symbols on Fig. 6) at various radial distances from the galaxy's centre along the galaxy's major axis (at the positions R_i with respect to galaxy's observed centre). We then compute the values for V_* and σ_* at the galaxy's outskirts (so in our case at $R = 0.2$ arcsec along the major axis). This procedure gives us the projected value of $(V/\sigma)_*$. In order to calculate the de-projected value we use equation (A.2) from J. Falcón-Barroso et al. (2019) and obtain $(V/\sigma)_* = 0.76 \pm 0.16$.

4.4.3 *Specific angular momentum parameter* $\lambda_{2R_{\rm eff}}$

Our resolution does not allow us to compute the spin parameter within 1 $R_{\rm eff}$ directly. We have only one Voronoi bin within 1 $R_{\rm eff}$ (out of the 17 Voronoi bins) but six Voronoi bins within 2 $R_{\rm eff}$ of the galaxy's centre. The radial distances of the Voronoi bin 'k' are $R_k = \sqrt{x_{\rm rot,k}^2 + y_{\rm rot,k}^2}$, where $x_{\rm rot}$ and $y_{\rm rot}$ are the Voronoi bins coordinates in the rotated system. We do not correct for inclination at this step yet as we will do the de-projection calculations at a later step. The spin parameter within 2 $R_{\rm eff}$ can be computed by summing over the Voronoi bins within the said aperture. For the resolved stellar kinematics maps of the galaxy, V_k and σ_k, we use the output stellar kinematics maps from the *JAM* fiducial dynamical model. Following the definition from E. Emsellem et al. (2007):

$$\lambda_{2R_{\rm eff}} = \frac{\sum_{k}^{R_k<2R_{\rm eff}} F_k R_k \left|V_k\right|}{\sum_{k}^{R_k<2R_{\rm eff}} F_k R_k \sqrt{V_k^2 + \sigma_k^2}}. \tag{11}$$

In this equation F_k represents the light flux at the position of the Voronoi bin. This light flux distribution map can be obtained as a direct output of our *JAM* dynamical model, but an alternative method is to simply add up all the signal from the pixels contained within each Voronoi bin. We chose to use the former method because it ensures better consistency with the input light maps that were used for *JAM*. However, in order to estimate the uncertainties on the Voronoi bin fluxes, F_k, we proceeded by first creating a pseudo-NIRCam $F200W$ band image of our target in order to mimic the photometric data from which the light maps inputs for *JAM* were constructed. Each Voronoi bin spectrum was convolved with the transmission curve $\mathcal{T}(\lambda)$ of the $F200W$ band[11] such that for any wavelength slice λ_j:

$$F_{\rm bin\,k,pseudo} = \sum_j F_{\rm bin\,k}\left(\lambda_j\right) \times w\left(\lambda_j\right), \tag{12}$$

[11] Information about the NIRCam filters can be found here.

with the wavelength slices weights defined as $w(\lambda_j) = \mathcal{T}(\lambda_j) / \sum_i \mathcal{T}(\lambda_i)$. The noise values associated with the pseudo-$F200W$ images are calculated using

$$N_{\text{bin k,pseudo}} = \sqrt{\sum_j N^2_{\text{bin k}}(\lambda_j) \times w^2(\lambda_j)}. \quad (13)$$

As a result, we will approximate the uncertainties on the *JAM* Voronoi bin fluxes as $N_{\text{bin k,real}} = F_k \times N_{\text{bin k,pseudo}}/F_{\text{bin k,pseudo}}$, which we will use to propagate the uncertainties on $\lambda_{2R_{\text{eff}}}$ from equation (11). Doing the calculations and the error propagations, we obtain the raw (not de-projected and not PSF corrected) $\lambda_{2R_{\text{eff}}} = 0.26 \pm 0.03$. In order to account for PSF effects, we use the empirical correction given by equations (9) and (16) from K. E. Harborne et al. (2020) and plugging in our values for observed ellipticity, Sérsic index, effective radius from Table 1, and $\sigma_{\text{PSF}} = 0.044$ arcsec, we obtain $\lambda_{2R_{\text{eff}}}$ (PSF corrected) $= 0.82 \pm 0.10$. This still needs to be corrected for de-projection effects, for which we use equation (A.3) from J. Falcón-Barroso et al. (2019, originally from E. Emsellem et al. 2011) and we obtain $\lambda_{2R_{\text{eff}}}$ (PSF corrected, deprojected) $= 0.85 \pm 0.10$.

Next, we can convert from $\lambda_{2R_{\text{eff}}}$ to $\lambda_{R_{\text{eff}}}$ using equation (2) from J. Falcón-Barroso et al. (2019): $\lambda_{2R_{\text{eff}}} = (1.19 \pm 0.14)\lambda_{R_{\text{eff}}}$. With this extrapolation, we would obtain $\lambda_{R_{\text{eff}}} = 0.72 \pm 0.09$. This $\lambda_{R_{\text{eff}}}$ value enables us to make comparisons with observations from the literature (see Section 5). The criterion to define a galaxy as a slow rotator was proposed as the equation (19) of M. Cappellari (2016): $\lambda_{R_{\text{eff}}} < 0.08 + \epsilon/4$. The intrinsic ellipticity of our galaxy is $\epsilon \approx 0.38$ in the *Fiducial* dynamical model. This certainly places our galaxy well within the fast rotator regime. We can instead consider the alternative criterion from E. Emsellem et al. (2011): $\lambda_{R_{\text{eff}}} > 0.31\sqrt{\epsilon}$ for $z \sim 0$ fast rotators. In this case, we reach the same conclusion that GS-9209 is definitely a fast rotator. This is further illustrated by calculating the value for $(V/\sigma)_{R_{\text{eff}}} = 0.93 \pm 0.27$ (obtained from $\lambda_{R_{\text{eff}}}$ by using equation 18 from M. Cappellari 2016) is in agreement, within the uncertainties, with the value computed in Section 4.4.2.

4.4.4 $\kappa_{\text{rot},*}$

We want to compute how much of the total kinetic energy budget of our galaxy goes into stellar ordered rotation. This parameter is defined using the equation (1) of L. V. Sales et al. (2012). In order to determine its value in our case, we use the JAM.AXI.INTR routine, which computes the intrinsic first and second velocity moments for an arbitrary axisymmetric galaxy model.

The first step is to compute the light and the dark matter components *MGE* parametrization. For a Gaussian with a peak surface brightness I_k, dispersion σ_k, and observed axial ratio q'_k, and intrinsic axial ratio q_k (see Section 3.1.2 for details), the luminosity density is (equation 38 from M. Cappellari 2020):

$$\nu_k = \frac{I_k q'_k}{q_k \sigma_k \sqrt{2\pi}}. \quad (14)$$

In our case, for all Gaussians of the light component in our parametrization $q'_k = 0.749$ and $q_k = q_{\text{intr}} = 0.62$. For the dark matter component, we fit the classic NFW density profile (equation 5) using MGE_FIT_1D in a similar way to how we fit the Sérsic profile in Section 3.1.2 for the luminuous component. The resulting best-fitting peak surface densities of the DM Gaussians are converted to volume densities using again the equation (14) and assuming a spherical dark matter halo so for all of these Gaussians $q'_{\text{DM}} = q_{\text{DM}} = 1$. We next use the JAM.MGE.RADIAL_MASS function in order to calculate the amount of luminous mass within the effective radius in order to scale the dark matter component in such a way that $f_{\text{DM}}\,(< 2R_{\text{eff}})$ matches the result from our *Fiducial* dynamical model (14.5 per cent). Combining the *MGE* Gaussians for these two components, we obtain the gravitational potential parametrization for our dynamical model that will be passed as input to JAM.AXI.INTR (together with the luminous component parametrization alone). We assume the central BH mass to be $10^{8.8}$ $M_\odot$ (A. C. Carnall et al. 2023b), the inclination angle is $i = 57.8^\circ$, and $\beta = 1 - \sigma_z^2/\sigma_R^2 = 0.286$ (both values are computed based on the results of the *Fiducial* dynamical model).

For our intrinsic dynamical model we use a grid in a cylindrical system of coordinates with $R = 0$ at the centre of the galaxy and $z = 0$ in the central plane of this galaxy. The points in the grid at which we evaluate the model span from $0.5\,R_{\text{eff}} < R < 20\,R_{\text{eff}}$ and from $-R_{\text{eff}}\sqrt{q_{\text{intr}}} < z < +R_{\text{eff}}\sqrt{q_{\text{intr}}}$ with 1000 equally spaced points in both R and z ranges. At each of these points, this model evaluates four quantities:

(i) $\sigma^2_{R,j}$, $\sigma^2_{z,j}$, $\sigma^2_{\phi,j}$, the squared velocity dispersions along the radial, vertical, and azimuthal directions.

(ii) $\langle v^2_\phi \rangle_j$, the second velocity moment along the tangential direction, which in turn gives us the mean velocity of rotation along the tangential direction $\langle v_\phi \rangle_j = \sqrt{\langle v^2_\phi \rangle_j - \sigma^2_{\phi,j}}$.

The equation (1) from L. V. Sales et al. (2012) can thus be rewritten as

$$\kappa_{\text{rot},*} = \frac{\sum_j \left(m_j \langle v_\phi \rangle^2_j \right)}{\sum_j \left[m_j \left(\sigma^2_{\text{R,j}} + \sigma^2_{\text{z,j}} + \langle v^2_\phi \rangle_j \right) \right]}. \quad (15)$$

The mass weights at each point of the (R, z) grid have been computed using equation (13) from M. Cappellari (2008) for the luminous component *MGE* parametrization and its analogous (equation 15 from M. Cappellari 2008) for the dark matter component Gaussians and for each point on the grid $m_j = \nu_{\text{lum}}(R_j, z_j) + \rho_{\text{DM}}(R_j, z_j)$. The total luminosity of a Gaussian with peak surface brightness I_k, dispersion σ_k, and observed axial ratio q'_k is $L_k = 2\pi q'_k \sigma^2_k I_k$ and the equation is completely analogous for the total mass of a DM Gaussian. Using our results for these quantities, we obtain $\kappa_{\text{rot},*} = 0.39 \pm 0.08$.

5 DISCUSSION

5.1 Dynamical structure of GS-9209

In this subsection, we discuss the properties of GS-9209 resulting from our dynamical model. We combine this information with the findings of our kinematics analysis in order to infer the most likely scenarios for the mass assembly history for this galaxy. In A. C. Carnall et al. (2023b), the authors justify, based on their model SFH, that $z \sim$ 3-5 MQGs have likely gone through a starburst/sub-millimetre galaxy (SMG) phase prior to the observation epoch. Therefore, we will now focus on exploring what the possible low-redshift descendants of MQGs like GS-9209 might be.

5.1.1 Dark matter content-comparison with local observations

In the corner plot of Fig. 5, we estimate a dark matter mass fraction within $2\,R_{\rm eff}$ of $14.5^{+6.0}_{-4.2}$ per cent. Because we assume a classical NFW dark matter density profile, this allows us to subsequently extrapolate the fraction of DM within one effective radius: $f_{\rm DM}\,(<R_{\rm eff}) = 6.3^{+2.8}_{-1.7}$ per cent, although it is crucial to stress that this quantity is obtained indirectly, because the spatial resolution of our data do not allow us to directly measure this quantity or the precise shape of the inner DM profile.

We compare this inferred low dark matter fraction that we found for GS-9209 (within 1 $R_{\rm eff}$) with the values reported by a number of observational studies. M. Cappellari et al. (2013a) analyse a sample of local ETGs within the ATLAS$^{\rm 3D}$ survey and conduct *JAM* dynamical modelling of these galaxies, finding a median $f_{\rm DM}\,(<R_{\rm eff}) \sim 13$ per cent for their entire sample, but only about ~ 9 per cent for their most robustly modelled galaxies. S. Lu et al. (2024) have a 20 times larger sample of low-redshift ETGs and conduct a similar *JAM* dynamical modelling analysis, obtaining that the average $f\,(<R_{\rm eff}) \approx 10$ per cent for $\sigma_e > 10^{2.1}$ km s^{-1}. S. Shetty & M. Cappellari (2015) also find a median $f_{\rm DM}\,(<R_{\rm eff}) = 9$ per cent for a sample of massive galaxies ($10^{10}{\rm M}_\odot < M_* < 10^{12}{\rm M}_\odot$) at $z \sim 0.8$. For the higher redshift sample of $1.4 < z < 2.0$ MQGs of J. T. Mendel et al. (2020), the average DM fraction within the effective radius is lower (6.6 per cent on average) compared with their likely local descendants. This is in line with the predictions of simulations such as M. Hilz, T. Naab & J. P. Ostriker (2013), who find that $f_{\rm DM}\,(<R_{\rm eff})$ increases as galaxies build up their stellar mass via mergers throughout their evolution. Hence, $f_{\rm DM}\,(<R_{\rm eff})$ is also predicted to increase with cosmic time. In the case of post-Cosmic Noon major mergers, the increase is mild and mainly driven by mixing processes leading to an intrinsic change in the spatial distribution of light and dark matter components (M. Hilz et al. 2012). However, minor mergers will lead to a more substantial increase in $\rm f_{DM}\,(<R_{eff})$ because in this case, the increase in stellar effective size is significant (C. Nipoti, T. Treu & A. S. Bolton 2009), meaning that now $R_{\rm eff}$ probes more extended regions of the dark matter halo (hence with more dark matter mass). Possible colour gradients could also have an impact, since the outskirts of MQGs are dominated by younger stellar populations (assuming an inside-out quenching scenario) hence with lower M_*/L ratios. This was proved to be true for GS-9209 (Z. Ji et al. 2024b) with the galaxy's outskirts at $r > 0.3$ arcsec from the centre being younger than the central region at $r < 0.3$ arcsec. Since our kinematics data only extend up to 0.2 arcsec and our dark matter fractions are measured within apertures lower than 0.2 arcsec, this means that the gradient discovered by Z. Ji et al. (2024b) was probed on larger spatial scales and our assumption of spatially uniform M_*/L is still valid.

We provide a comparison between the dark matter fraction of GS-9209, $f_{\rm DM}\,(<2\,R_{\rm eff})$, and the predictions of numerical simulations (focusing on the *TNG50-1* simulation box) in Appendix E.

5.1.2 Extremely compact nature and possible descendants of GS-9209

Compact stellar sizes were reported for individual MQGs (A. C. Carnall et al. 2023b; A. Graaff et al. 2024; A. Weibel et al. 2025) but also for sample studies (K. Ito et al. 2024; L. Wright et al. 2024; Z. Ji et al. 2024a). It means that prior to quenching, the cold gas fuelling the extreme star formation episodes in the history of such galaxies was either channelled to the galaxy's innermost central part (this is in agreement with the findings of previous studies based on cosmological simulations, e.g. A. Zolotov et al. 2015; S. Tacchella et al. 2016; W. McClymont et al. 2025) or that a compaction episode happened post-quenching: when the gas in the original stellar disc was consumed and the turbulent motions disappeared, the stellar orbits got shrinked as a result of dynamical friction. The rotation pattern of the stellar component observed in GS-9209 tells us that the stellar disc is not destroyed by the quenching mechanism (at least not immediately). This seems to be in agreement with the inside-out quenching scenario (S. Tacchella & others 2015) and it tells us that the formation of spheroid components takes place on a much longer time-scale compared to quenching in the case of MQGs in the early Universe.

The presence of a rotational pattern in the V_* resolved map of this galaxy further indicates that this galaxy assembled most of its stellar mass, not by dry major mergers but more likely via secular accretion of cold gas possibly channelled along the cosmic web filaments (which ensures transportation of the gas deeper towards the central regions of massive haloes). This picture is, however, challenged by the findings of L. C. Kimmig et al. (2025) who argue in the favour of the hypothesis that high-redshift MQGs may have initially been local nodes of the cosmic web residing in underdense environments. This means that the local filamentary structure is unable to efficiently accumulate mass at the node, leading to an extreme episode of isotropic spherical mass accretion on to the node, which is followed by a strong starburst phase. In any case, the subsequent quenching is likely the result of the action of AGN ejective feedback driving large outflows of cold gas, which is rapidly expelled out of the galaxy's circumgalactic medium. Preventative feedback causes the heating of the gas in the halo, which ensures the long-term quiescence of galaxies such as GS-9209 or ZF-UDS-7329 (K. Glazebrook et al. 2024).

Gas-rich mergers (either major or minor) must also take place (likely before the quenching event) in the case of GS-9209, since this galaxy is somewhat rounder compared to both the average local and high-z pure discs. C. d. P. Lagos et al. (2018) show that gas-rich mergers typically produce small changes in a galaxy's stellar specific angular momentum and, in some cases, it might even cause a galaxy to spin-up. Dry major mergers, however, are less plausible since they would distort or even destroy the stellar rotation pattern that we observe. This seems to be in agreement with the findings of D. Puskás et al. (2025) who determine that major mergers contribute less than 15 per cent to galaxies' stellar mass growth (in a redshift range $3 < z < 9$ and for a sample with stellar masses $8 < \log(M_*/{\rm M}_\odot) < 10$). Such galaxies could be the progenitors of MQGs like GS-9209. Numerical simulations (e.g. S. Tacchella et al. 2019) reveal that *ex situ* processes become the dominant source of mass growth in the case of massive $M_* > 10^{11}$ M$_\odot$ galaxies only at lower redshifts $z < 2$. Q. Duan et al. (2025) find that at the redshift of GS-9209, the merger rate per galaxy is about 2 Gyr^{-1} on average. A. C. Carnall et al. (2023b) calculate that the age of this galaxy at the observation time (i.e. $t_{\rm obs} - t_{\rm form}$) is 400−500 Myr. Thus, all these results support the possibility that GS-9209 has not undergone a significant major merger throughout its history prior to $z = 4.66$. However, any major mergers in the subsequent evolution of MQGs like GS-9209 will ultimately determine the possible descendants of early formed early quenched massive galaxies.

Due to the high-z MQGs' compactness, many authors claimed them to be the progenitors of the compact dense cores of Cosmic Noon and later ETGs (A. C. Carnall et al. 2023b; Z. Ji et al. 2024c;

A. Weibel et al. 2025). Indeed, correlations between quenching and $M_{\rm bulge}$ exist (M. Cappellari et al. 2013b; A. F. L. Bluck et al. 2014) and, furthermore, by $z \approx 2.5$ there is clear evidence for massive bulges and galaxies with suppressed star formation, at least in their core regions (S. Tacchella et al. 2015). However, it is likely that a fraction of high-redshift compact MQGs similar to GS-9209 may not be involved in low-redshift major mergers. They might be the progenitors of a rare class of compact massive ETGs known as 'relics'. An example of such a galaxy is NGC 1277 (I. Trujillo et al. 2014; S. Comerón et al. 2023), which has seen little change in terms of its stellar populations or structural properties within the last 12 Gyr. Further evidence that internal processes have the largest contribution to the mass assembly of NGC 1277 is represented by the discovery that this galaxy predominantly hosts metal-rich (red) globular clusters (M. A. Beasley et al. 2018). The stellar populations of relic galaxies are believed to be formed during a single starburst episode in the history of this galaxy. M. A. Beasley et al. (2018) find that the fraction of blue metal-poor globular clusters in NGC 1277 (whose likely origin is accretion from less massive companion galaxies) is significantly smaller compared to galaxies of similar M_* to NGC 1277.

Regarding the dark matter content, NGC 1277 is even more baryon dominated ($f_{\rm DM}\,(<5\,R_{\rm eff}) < 5$ per cent) than GS-9209. Both NGC 1277 and GS-9209 are fast rotators, highly compact and strongly baryon dominated, indicating that the latter galaxy is the currently highest-redshift analogue of the local relics galaxy population. A possible link between high-redshift MQGs and low-redshift relics has been suggested by E. A. Hartmann et al. (2025). S. Comerón et al. (2023) suggest that the low dark-matter content of relics in the local Universe might be caused by processes taking place in early stages of galaxy formation. One possible explanation could be that, during the early stages of massive galaxy formation, baryons cool and accrete on to the central galaxy on a shorter time-scale than dark matter. An alternative possibility is given by an extensive dark matter component stripping during the galaxy's infall into a rich galaxy cluster (NGC 1277 is part of the Perseus Cluster, but this does not apply to GS-9209, which is an isolated object). Finally, the low dark matter fraction could also be explained by an early proto-galactic collision that essentially left the galaxy heavily baryon dominated for its entire subsequent evolution.

Interestingly, GS-9209 and NGC 1277 possess a key difference: the IMFs of their stellar populations. S. Comerón et al. (2023) found an extremely bottom-heavy IMF with $\alpha = (M_*/L)\,/\,(M_*/L)_{\rm Salpeter} = 1.3$-$1.5$ for NGC 1277. A. Ferré-Mateu et al. (2017) also found that two additional relic galaxies (Mrk 1216 and PGC-032873) have bottom-heavy IMFs. Indeed, M. Maksymowicz-Maciata et al. (2024) reported (fig. 5 of their paper) that extreme relic galaxies are generally characterized by a bottom-heavy IMF. However, we find that GS-9209 is instead characterized by a standard IMF. This is because our fiducial dynamical model returned $\log(M_*/{\rm M}_\odot) = 10.52 \pm 0.06$, which is in excellent agreement with the value found by A. C. Carnall et al. (2023b) (10.58 ± 0.02) who performed an SED fitting of the galaxy's spectrum and assumed a Kroupa IMF (P. Kroupa 2001). This may point to some differences in the formation and mass assembly processes of early massive quenched galaxies, compared to low-redshift relic galaxies. Hence, it is unclear whether the former category truly represents the progenitors of the latter.

Regardless, our findings represent the first dynamical measurement of the IMF at $z > 3$, highlighting the potential of future spatially resolved surveys of high-redshift MQGs.

5.2 $\lambda_{R_{\rm eff}}$ Comparison with literature

Our value of $\lambda_{2R_{\rm eff}} = 0.85 \pm 0.10$ gives $\lambda_{R_{\rm eff}} = 0.72 \pm 0.09$ (as shown in Section 4.4.2). We can study the properties of GS-9209 by comparing it with GS-10578 (another MQG, but at lower redshift, $z \sim 3.064$). As we can observe in Fig. 7 these galaxies occupy a similar place in the $\lambda_{R_{\rm eff}} - \epsilon$ plane but they have quite different stellar masses. It is important to look in more detail at some potential key differences between the way these two galaxies assembled their mass and quenched star formation.

F. D'Eugenio et al. (2024) mention that GS-10578 had its main star formation episodes at epochs $z = 3.7$-4.6. The stellar mass of GS-10578 is approximately five times larger than that of GS-9209. Both galaxies retain high values of specific angular momentum, which means that these galaxies formed most of their stellar mass *in situ* and that they likely did not experience significant gas-poor mergers (otherwise we would not observe a significant stellar rotation; e.g. C. d. P. Lagos et al. 2018). If galaxies like GS-9209 were the direct progenitors of those like GS-10578, given the stellar mass differences between the two galaxies, and the difference in the ages of the Universe at these redshifts, this would imply an average stellar mass growth rate of $\dot{M}_* \geq 200\,{\rm M}_\odot\,{\rm yr}^{-1}$. If this was fuelled solely by fresh cold gas accretion (major mergers would disturb the observed stellar disc motions), that new reservoir of cold gas would need to be converted into stars in order to match the observational constraints of low molecular hydrogen mass fraction in $z > 3$ quiescent galaxies (e.g. T. L. Suzuki et al. 2022; J. Scholtz et al. 2024). Such high values of SFR are typically associated with high-redshift sub-millimetre galaxies (SMGs) or high-redshift dusty star-forming galaxies (DSFGs; S. Carniani et al. 2013; R. Gilli et al. 2014; Q. Tan et al. 2014; C. M. Casey et al. 2019; P. Sharda et al. 2019; D. A. Riechers et al. 2020; F. Rizzo et al. 2020, 2021; J. E. Birkin et al. 2021; F. Fraternali et al. 2021; S. Ikarashi et al. 2022; E. Parlanti et al. 2023; S. Arribas et al. 2024; M. Fuentealba-Fuentes et al. 2024; F. Sun et al. 2024; Y. Zhu et al. 2024; N. B. Sillassen et al. 2025). Consequently, a plausible explanation is that $z > 4$ SMGs and/or DSFGs could be the progenitors of MQGs like GS-9209 or GS-10578. Some galaxy formation and evolution simulations predict an evolutionary link between SMGs and MQGs (C. d. P. Lagos et al. 2015).

M. Park et al. (2024) analysed SFHs in Cosmic Noon MQGs and they report having found their sample to be split into three different sub-categories (fig. 7 of that paper). In our case, the findings of M. Park et al. (2024) resonate with the different SFHs of GS-10578 (which is a recently formed, recently quenched galaxy) and GS-9209 (an early formed, early quenched galaxy). As a result, despite showing some similarities, galaxies such as GS-9209 are unlikely to be the direct progenitors of those like GS-10578. This underlines the idea that the likely mechanisms of mass assembly and quenching of MQGs were already in place at $z > 5$ and, moreover, the same processes seem to occur in a similar way for widely different stellar masses.

Close similarity in terms of the position in the $\lambda_{R_{\rm eff}} - \epsilon$ plane can be observed in the case of the $z \sim 2$ galaxies MRG-M0138 and MRG-M2129. However, just as in the case of GS-10578 versus GS-9209, the stellar masses of these Cosmic Noon quiescent galaxies are also widely different: $M_* = 10^{10.96}{\rm M}_\odot$ for MRG-M2129 and $M_* = 10^{11.69}{\rm M}_\odot$ for MRG-M0138. In the case of these galaxies, the stellar rotation component (highlighted by the high ellipticity and high $\lambda_{R_{\rm eff}}$) has been preserved after quenching. In addition, the galaxies are observed (via lensing) at similar redshifts ($z \sim 2.15$ for MRG-M2129, S. Toft et al. 2017 and $z \sim 1.95$ for MRG-M0138, A. B. Newman et al. 2018b), which, given the highly

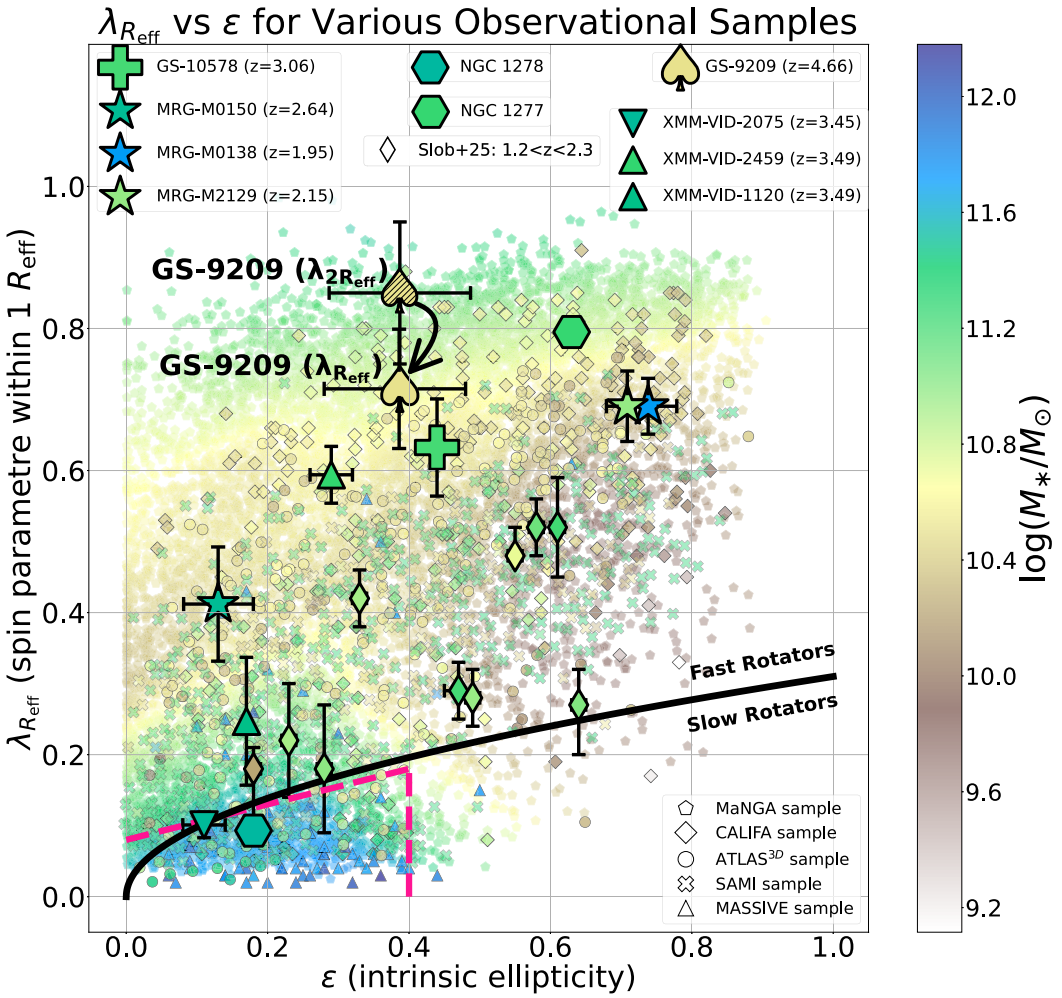

Figure 7. $\lambda_{R_{\rm eff}}$ against ellipticity, colour coded by log ($M_*/M_\odot$).**The small symbols** are galaxies from various observational surveys that offer a comprehensive picture of the kinematic properties of local galaxies with $M_* > 10^9$ $M_\odot$. The **small pentagons** are $z < 0.17$ galaxies from the MaNGA DynPop catalogue (K. Zhu et al. 2023). **The small diamonds** are local galaxies ($0.005 < z < 0.03$) from the *CALIFA* survey (J. Falcón-Barroso et al. 2019). **The small circles** represent E and S0 type galaxies in the nearby Universe from ATLAS^{3D} survey (M. Cappellari et al. 2011). For the purpose of their colour coding by stellar mass, we multiplied the *r*-band luminosity data from M. Cappellari et al. (2013a) with the stellar M/L ratio in the same band (from M. Cappellari & others 2013b). Because these three data sets are large, we *LOESS* smoothed (see W. S. Cleveland & S. J. Devlin 1988) each of them. The **X crosses** are $z < 0.095$ galaxies from *SAMI* survey (J. de Sande et al. 2017). **The small triangles** represent extremely massive ($M_* > 10^{11.5} M_\odot$) local ETGs from the *MASSIVE* sample (M. Veale et al. 2017a, b). We overplot the positions on this diagram of 10 MQGs near Cosmic Noon ($1.2 < z < 2.3$ from M. Slob et al. 2025; diamonds), three additional lensed MQGs at $z = 1.93$-2.64 (MRG sample; A. B. Newman et al. 2018b), two massive, dark matter-defficient galaxies, **NGC 1277 and NGC 1278** ($f_{\rm DM}(< 5R_{\rm eff}) < 0.05$ and $f_{\rm DM}(< 1.5R_{\rm eff}) = 0.14 \pm 0.04$, respectively) reported by S. Comerón et al. (2023) and, finally, three galaxies at $z \sim 3.5$ from the VISTA Deep Extragalactic Observations survey (VIDEO; M. J. Jarvis et al. 2013), including the earliest slow rotator known, XMM-VID-2075 (B. Forrest et al. 2025; downwards pointing triangle). GS-10578 (F. D'Eugenio et al. 2024) is the most similar fast rotator MQG to our target. The two fast/slow rotator boundaries follow the equations: $\lambda_{R_{\rm eff}} = 0.08 + \epsilon/4$ (for $\epsilon < 0.4$; M. Cappellari 2016, pink dashed line) and $\lambda_{R_{\rm eff}} = 0.31 \cdot \sqrt{\epsilon}$ (E. Emsellem et al. 2011, black solid line). In this plot, we also illustrate the empirical relation $\lambda_{2R_{\rm eff}} = (1.19 \pm 0.14) \times \lambda_{R_{\rm eff}}$ (J. Falcón-Barroso et al. 2019) that we used to estimate the observationally inaccessible $\lambda_{R_{\rm eff}}$ (due to spatial resolution limitations) based on our measurement of $\lambda_{2R_{\rm eff}}$. Admittedly, this empirical correction is not perfect, but it is accurate enough to preserve our conclusion that GS-9209 is unambiguously a fast rotator.

different stellar masses, argues for different SFHs in these galaxies. Again, given the high $\lambda_{R_{\rm eff}}$, it is most likely that these galaxies built most of their stellar masses via secular cosmological gas accretion and *in situ* gas conversion into stars. Nevertheless, the quenching mechanism leading to the halting of star formation in such massive galaxies seem to be taking place in a similar way independent of M_*. It can be remarked that the MQGs at $z > 1.5$ that we plotted in Fig. 7 and the relic galaxy NGC 1277 at $z = 0$ are all fast-rotators. This is in very good agreement with the findings from the *Magneticum Pathfinder* simulations. Fig. 10 from L. C. Kimmig et al. (2025) highlights that at all redshifts $2.7 < z < 5.4$ tested by the authors, slow rotators quiescent galaxies represent a minority of the overall galaxy population.

5.3 V/σ Comparison with observations

In Fig. 8, we plot the evolution of the ratio between stellar rotational velocity and stellar velocity dispersion ($V/\sigma \equiv$ V ($R_{\rm eff}$) /σ_0) based various observational samples. We present the quiescent galaxies in the *LEGA-C* and *SUSPENSE* samples, together with the six MQGs at $z > 1.5$, which have available stellar

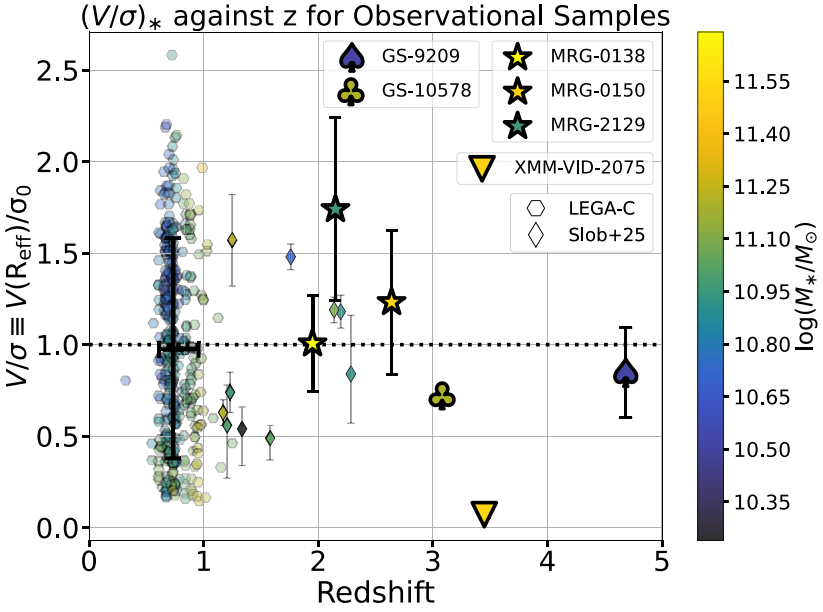

Figure 8. This figure illustrates the ratios of rotational velocity to velocity dispersion, $(V/\sigma)_*$ as traced by stellar kinematics of various targets at $0.5 < z < 5$. All targets are colour coded using the logarithm of the stellar mass. GS-9209 (presented in this work) is the highest-redshift object for which this measure of rotational support was determined. **The background hexagons** are $0.6 < z < 1$MQGs whose stellar kinematics were determined with Jeans anisotropic models (J. Houdt et al. 2021). The two thick error bars indicate the median redshift and $V_{R_{\rm eff}}/\sigma_0$, together with their [5; 95] per cent and [16; 84] per cent ranges, respectively. **The 10 small diamonds** are a sample of MQGs near Cosmic Noon ($1.2 < z < 2.3$) from the *SUSPENSE* survey (M. Slob et al. 2025). We also overplot the three lensed MQGs at $1.95 < z < 2.64$ from A. B. Newman et al. (2018b), the recently discovered massive slow rotator at $z = 3.45$ (XMM-VID-2075; B. Forrest et al. 2025) and the GS-10578 (F. D'Eugenio et al. 2024) fast-rotator, with the most similar kinematic properties to GS-9209. The existence of XMM-VID-2075 slow rotator is surprising, given that most of the other $z > 1$ MQGs are fast rotators. The existing observational data are too scarce to constrain an evolutionary trend with redshift, but excluding XMM-VID-2075, the other data points shown here seem to indicate that the stellar V/σ ratio does not evolve sigificantly across cosmic time.

kinematics data. In cases where $V(R_{\rm eff})/\sigma_0$ is not directly reported, we compute this ratio as follows. For five of our individual MQGs highlighted in the plot (GS-9209, GS-10578 from F. D'Eugenio et al. 2024, MRG-0138, MRG-0150, and MRG-2129 from A. B. Newman et al. 2018b), we use their radial profiles of the velocity dispersion σ (R) to determine the ratio $\sigma(R=0)/\sigma(R=R_{\rm eff})$. In the case of the slow rotator XMM-VID-2075, B. Forrest et al. (2025) report $\sigma_0 \sim 500$ km s^{-1} and $\sigma_{R_{\rm eff}} = 387 \pm 22$ km s^{-1}, from which we obtain a value of 1.29 ± 0.07 for this ratio. We then estimate the values of $(V/\sigma)_{R_{\rm eff}}$ based on the measured $\lambda_{R_{\rm eff}}$ parameters using equation (18) from M. Cappellari 2016. We then multiplied $(V/\sigma)_{R_{\rm eff}}$ by $\sigma(R_{\rm eff})/\sigma_0$. The existence of a slow rotator MQG at $z \sim 3.44$ could be potentially explained as the outcome of a major merger event, which strongly disrupted a previously existing stellar disc. This would also be consistent with the relatively high observed axial ratio of that object ($q' \sim 0.89$; B. Forrest et al. 2025). However, an alternative hypothesis of an isotropic gas infall has been proposed by Á. Chandro-Gómez et al. (2025).

For the three lensed massive quiescent targets from A. B. Newman et al. (2018b), their effective radii are given in A. B. Newman et al. (2018a) in the case of MRG-2129 and MRG-0150 and in A. B. Newman et al. (2025) for MRG-0138. We have assumed that for these three MQGs $\sigma_0 \approx \sigma(R=0)$. This approximation is true in the case of GS-9209 ($\sigma'_* \approx 239 \pm 34$ km s^{-1}, see Section 3.2; $\sigma'(R=0) \approx$ 230-240 km s^{-1}, see Fig. 6). The numerical uncertainty of the aperture-integrated velocity dispersion that we measure is larger than the difference between σ'_* and $\sigma'(R=0)$ by an order of magnitude.

In the case of quiescent galaxy samples with stellar kinematics, there is no significant trend between $(V/\sigma)_*$ and redshift (see Fig. 8). However, this sample of $z > 2$ MQGs, together with the quenched galaxies from *LEGA-C* and *SUSPENSE*, is not large enough to obtain a statistically significant conclusion. Within the *LEGA-C* sample, lower mass quiescent galaxies have more rotational support. This is in contrast with the findings of $z < 3$ ionized gas kinematics surveys targetting star-forming galaxies (E. Wisnioski et al. 2015, 2019; R. C. Simons et al. 2016; N. M. Förster Schreiber et al. 2018; R. Genzel et al. 2020); in these cases, the galaxies with the highest V/σ ratios are also very massive (E. Wisnioski et al. 2019; A. L. Danhaive et al. 2025). This highlights the different behaviour of distinct kinematics tracers (e.g. star and warm ionized gas, in this case), which furthermore implies that $(V/\sigma)_*$ and $(V/\sigma)_*$ cannot be compared directly. This is because ionized gas typically traces a more dynamically active interstellar medium, while the stars in fast-rotators MQGs like GS-9209 or GS-10578 have reached a steady-state ordered rotation.

6 CONCLUSIONS

In this paper, we used ultra-deep (14.7 h) high-resolution IFU *JWST*/NIRSpec data with the G235H grating to conduct a detailed analysis of the structural, kinematic and dynamic properties of the $z \sim 4.66$ MQG GS-9209.

(i) From the integrated aperture spectrum, we measure a stellar velocity dispersion of $\sigma'_* = 239 \pm 34$ km s^{-1} in agreement with the value found by A. C. Carnall et al. (2023b) (247 ± 16 km s^{-1}, obtained using medium-resolution spectroscopy).

(ii) We showed the resolved maps V_* and σ_*, extending out to ~ 6 $R_{\rm eff}$ ~ 1.3 kpc. The stellar velocity map shows clear evidence for ordered rotation, which makes GS-9209 the highest-redshift galaxy for which such a feature is probed via integral field spectroscopy.

(iii) We find that GS-9209 is rotation supported, having a high (PSF-corrected) $\lambda_{2R_{\rm eff}} = 0.85 \pm 0.10$, from which we can extrapolate that $\lambda_{R_{\rm eff}} = 0.72 \pm 0.09$, comparable to other quiescent galaxies at $z = 2$-3. This value of $\lambda_{R_{\rm eff}}$ is equivalent to a $(V/\sigma)_{R_{\rm eff}} = 0.93 \pm 0.27$. This means that the mechanism responsible for quenching this galaxy still preserved the rotating stellar disc. GS-9209 is a fast rotator similar to other intermediate and high-z MQGs (A. B. Newman et al. 2018b; F. D'Eugenio et al. 2024). Furthermore, the high degree of rotational support suggests that the kinematic transformation between fast and slow rotators observed at lower redshifts occurs only after quenching. This is in agreement with the results obtained from numerical simulations: quenching preceedes kinematic transformation in galaxies that become slow rotators at $z \sim 0$ (S. Tacchella et al. 2019; C. d. P. Lagos et al. 2022).

(iv) We then fit our fiducial dynamical model (with a classical NFW DM profile and a BH whose mass takes a Gaussian prior motivated by virial scaling relations based on its broad-line Hα emission properties). The model assumes a cylindrical alignment of the velocity ellipsoid. With our fiducial dynamical model, we obtain the currently highest-redshift measurement of the dark matter content of a galaxy based on its stellar kinematics: $f_{\rm DM}\,(< 2R_{\rm eff}) = 14.5^{+6.0}_{-4.2}$ per cent. Given the compact nature of the source (compared to e.g. its host dark matter halo) the low DM fraction is in line with the expectations. Other important parameters that come out from the dynamical modelling are the intrinsic axial ratio and the radial anisotropy. These are crucial in our de-projection calculations for the kinematics parameters.

(v) Also from our fiducial dynamical model, we infer a $(M_*/L) = 0.10 \pm 0.02\,{\rm M}_\odot/L_\odot$. This represents the first such measurement at $z > 2$ and it is consistent with a standard Milky Way-like IMF from stellar population modelling. The agreement with the value inferred from SED modelling (A. C. Carnall et al. 2023b) provides independent confirmation on the large stellar mass of early quiescent galaxies.

(vi) The low dark matter content of GS-9209 and its high spin parameter make it similar to the $z \sim 0$ population of relic galaxies (e.g. S. Comerón et al. 2023). This remarkable category of galaxies has undergone little evolution within a time interval of ~ 10 Gyr or more. However, one possible key difference between high-redshift MQGs and low-redshift relics is the difference between their IMFs. Further dynamical studies on high-z MQGs would reveal their IMFs, which could confirm or refute the possibility of them being the progenitors of low-redshift relic galaxies.

(vii) We compared the value of $\lambda_{R_{\rm eff}}$ of GS-9209 (corrected for projection and PSF effects) to independent observational surveys in the $z < 1$ Universe but also to various $z > 2$ particular MQGs for which this parameter was calculated. For virtually all intermediate and high-z MQGs (except for one recently discovered high-redshift slow rotator) the positions on the $\lambda_{R_{\rm eff}}$-ϵ plane indicate that they are fast rotators. This is a strong evidence that the star formation quenching and the destruction of the stellar disc likely happen in this precise order. The causality relation between these two important milestones in a galaxy's evolution is yet to be fully understood. For the general galaxy population, as they build up their stellar mass, the amount of rotational support diminishes. This is in good agreement with the current galaxy evolution theories (e.g. F. Schulze et al. 2018 analyse the evolution of $\lambda_{R_{\rm eff}}$-ϵ plane at $z < 2$ in the MAGNETICUM simulations, reporting an increased fraction of slow rotators). This is correlated with the formation and growth of central bulges and dispersion-dominated spheroidal sub-structures.

The difficulty encountered by multiple simulations to reproduce the observed number density of MQGs and their physical properties (the most problematic one being the compact size) points to key differences between the processes governing the evolution of galaxies within $t < 1$ Gyr and the ones implemented in theoretical models. By exploring these differences, we can improve our understanding of the complex physical processes shaping the SFHs of high-redshift galaxies, their mass assembly histories, and the spatial distribution of baryons. In this direction, our work highlights the crucial ability of stellar kinematics data to provide constraints for cosmological simulations. From an observational point of view, studying quiescent galaxies enables us to measure their dark matter content without the complication of a possible large gas fraction such as in star-forming galaxies. Constructing a sample of high-redshift quenched galaxies with spatially resolved stellar kinematics would provide tighter constraints on current theoretical models.

In the absence of galactic outflows, this galaxy could be able to rejuvenate in the future via merger induced starbursts, for instance. The analysis of spatially resolved outflow properties in high-z MQGs could give more clear insights into their possible descendants. Another possible study would also involve FIR/sub-mm observations of this galaxy with ALMA, having the primary goal of investigating the amount of cold molecular gas and the state of that gas. This can be done with the [CII] λ158μm fine structure emission line or with CO emission lines, which are both tracers of molecular gas even for quiescent galaxies (C. D'Eugenio et al. 2023). Such studies can be extended to samples of multiple MQGs at $z > 2$, which would allow us to determine both the cold gas content and the gas-consumption histories of MQGs more accurately. This is because high-redshift MQGs are usually quenched close (less than 1 Gyr) to the observation time, so passive evolution effects are minimal, which puts more stringent constraints on the nature of the quenching mechanism. Such a sample could be compared with the results of numerical simulations (e.g G. Lorenzon et al. 2025) and thus provide an extremely valuable step forward in constraining the physics implemented in the next generation of galaxy evolution simulations.

ACKNOWLEDGEMENTS

We are grateful to the referee for insightful and constructive feedback that substantially improved the quality of this manuscript. RGP acknowledges funding support from a STFC PhD studentship. RGP, FDE, RM, and JS acknowledge support by the Science and Technology Facilities Council (STFC), by the ERC through Advanced Grant 695671 'QUENCH', and by the UKRI Frontier Research grant RISEandFALL. RM also acknowledges funding from a research professorship from the Royal Society. ST acknowledges support from the Royal Society Research Grant G125142. SC acknowledges support by European Union's HE ERC Starting Grant No. 101040227-WINGS. AJB acknowledges funding from the 'FirstGalaxies' Advanced Grant from the European Research Council (ERC) under the European Union's Horizon 2020 research and innovation program (Grant Agreement No. 789056). SA and MP acknowledge grant PID2021-127718NB-I00

funded by the Spanish Ministry of Science and Innovation/State Agency of Research (MICIN/AEI/ 10.13039/501100011033); MP also acknowledges the grant RYC2023-044853-I, funded by MICIU/AEI/10.13039/501100011033 and European Social Fund Plus (FSE+). We thank William Baker and Yuki Isobe for insightful discussions that led to improvements of the original manuscripts and paper drafts.

DATA AVAILABILITY

This work is based on observations conducted with the NASA/ESA/CSA James Webb Space Telescope. The data were obtained as part of the JWST program ID 3659 (Cycle 2, PI: Francesco D'Eugenio). The raw data are available from Mikulski Archive for Space Telescopes at the Space Telescope Science Institute, which is operated by the Association of Universities for Research in Astronomy, Inc., under NASA contract NAS 5-03127 for JWST. The fully reduced data cube is available via the following DOI: 10.5281/zenodo.18623840. The photometry data in the JWST/NIRCam F200W band are available from the public data release page of the JADES survey on MAST.

REFERENCES

Abraham R. G., 1999, Ap&SS, 269-270, 323
Alberts S. et al., 2024, ApJ, 975, 85
Arribas S. et al., 2024, A&A, 688, A146
Astropy Collaboration, 2022, ApJ, 935, 167
Baker W. M. et al., 2025a, MNRAS, 539, 557
Baker W. M. et al., 2025b, A&A, 702, A270
Barnabè M. et al., 2012, MNRAS, 423, 1073
Beasley M. A., Trujillo I., Leaman R., Montes M., 2018, Nature, 555, 483
Behroozi P. S., Wechsler R. H., Conroy C., 2013, ApJ, 770, 57
Belfiore F. et al., 2019, AJ, 158, 160
Belli S. et al., 2021, ApJ, 909, L11
Belli S. et al., 2024, Nature, 630, 54
Bentz M. C., Williams P. R., Treu T., 2022, ApJ, 934, 168
Beverage A. G., Kriek M., Conroy C., Bezanson R., Franx M., van der Wel A., 2021, ApJ, 917, L1
Beverage A. G., Kriek M., Conroy C., Sandford N. R., Bezanson R., Franx M., van der Wel A., Weisz D. R., 2023, ApJ, 948, 140
Bezanson R. et al., 2022, ApJ, 925, 153
Birkin J. E. et al., 2021, MNRAS, 501, 3926
Blanton M. R., Moustakas J., 2009, ARA&A, 47, 159
Bluck A. F. L., Mendel J. T., Ellison S. L., Moreno J., Simard L., Patton D. R., Starkenburg E., 2014, MNRAS, 441, 599
Bluck A. F. L., Maiolino R., Sánchez S. F., Ellison S. L., Thorp M. D., Piotrowska J. M., Teimoorinia H., Bundy K. A., 2020a, MNRAS, 492, 96
Bluck A. F. L. et al., 2020b, MNRAS, 499, 230
Böker T. et al., 2022, A&A, 661, A82
Bower R. G. et al., 2006, MNRAS, 370, 645
Bower R. G., Benson A. J., Crain R. A., 2012, MNRAS, 422, 2816
Bradley L. et al., 2024, astropy/photutils: 2.0.2, Zenodo
Brennan R. et al., 2017, MNRAS, 465, 619
Brownson S. et al., 2019, MNRAS, 490, 5134
Bugiani L. et al., 2025, ApJ, 981, 25
Cappellari M., 2002, MNRAS, 333, 400
Cappellari M., 2008, MNRAS, 390, 71
Cappellari M., 2016, ARA&A, 54, 597
Cappellari M., 2017, MNRAS, 466, 798
Cappellari M., 2020, MNRAS, 494, 4819
Cappellari M., 2023, MNRAS, 526, 3273
Cappellari M., Copin Y., 2003, MNRAS, 342, 345
Cappellari M., Emsellem E., 2004, PASP, 116, 138
Cappellari M. et al., 2006, MNRAS, 366, 1126
Cappellari M. et al., 2007, MNRAS, 379, 418
Cappellari M. et al., 2009, ApJ, 704, L34
Cappellari M. et al., 2011, MNRAS, 413, 813
Cappellari M. et al., 2013a, MNRAS, 432, 1709
Cappellari M. et al., 2013b, MNRAS, 432, 1862
Carnall A. C. et al., 2023a, MNRAS, 520, 3974
Carnall A. C. et al., 2023b, Nature, 619, 716
Carnall A. C. et al., 2024, MNRAS, 534, 325
Carniani S. et al., 2013, A&A, 559, A29
Casey C. M. et al., 2019, ApJ, 887, 55
Chandro-Gómez Á. et al., 2025, preprint (arXiv:2512.16208)
Choi J., Dotter A., Conroy C., Cantiello M., Paxton B., Johnson B. D., 2016, ApJ, 823, 102
Ciotti L., Bertin G., 1999, A&A, 352, 447
Cleveland W. S., Devlin S. J., 1988, J. Am. Stat. Assoc., 83, 596
Comerón S. et al., 2023, A&A, 675, A143
Conroy C., Gunn J. E., 2010, ApJ, 712, 833
Conroy C. et al., 2009, ApJ, 699, 486
Conroy C., Naidu R. P., Zaritsky D., Bonaca A., Cargile P., Johnson B. D., Caldwell N., 2019, ApJ, 887, 237
Cortese L., Catinella B., Smith R., 2021, Publ. Astron. Soc. Aust., 38, e035
Croom S. M. et al., 2024, MNRAS, 529, 3446
Croton D. J. et al., 2006, MNRAS, 365, 11
D'Eugenio C., Daddi E., Liu D., Gobat R., 2023, A&A, 678, L9
D'Eugenio F. et al., 2024, Nat. Astron., 8, 1443
D'Eugenio F. et al., 2025, ApJS, 277, 4
Danhaive A. L. et al., 2025, MNRAS, 543, 3249
Davé R., Anglés-Alcázar D., Narayanan D., Li Q., Rafieferantsoa M. H., Appleby S., 2019, MNRAS, 486, 2827
de Graaff A., Trayford J., Franx M., Schaller M., Schaye J., van der Wel A., 2022, MNRAS, 511, 2544
de Graaff A. et al., 2025, Nat. Astron., 9, 280
Decarli R., Dotti M., Treves A., 2011, MNRAS, 413, 39
Dekel A., Birnboim Y., 2006, MNRAS, 368, 2
Dekel A., Sarkar K. C., Birnboim Y., Mandelker N., Li Z., 2023, MNRAS, 523, 3201
Di Matteo T., Springel V., Hernquist L., 2005, Nature, 433, 604
Dimauro P. et al., 2022, MNRAS, 513, 256
Drehmer D. A., Storchi-Bergmann T., Ferrari F., Cappellari M., Riffel R. A., 2015, MNRAS, 450, 128
Du R., Ho L. C., Ding Y., Li R., 2025, ApJ, 988, 3
Duan Q. et al., 2024, preprint (arXiv:2411.04944)
Duan Q. et al., 2025, MNRAS, 540, 774
Eisenstein D. J. et al., 2023, preprint (arXiv:2306.02465)
Eisenstein D. J. et al., 2025, ApJS, 281, 50
Emsellem E., Monnet G., Bacon R., 1994, A&A, 285, 723
Emsellem E. et al., 2007, MNRAS, 379, 401
Emsellem E. et al., 2011, MNRAS, 414, 888
Falcón-Barroso J. et al., 2011, A&A, 532, A95
Falcón-Barroso J. et al., 2019, A&A, 632, A59
Feldmeier-Krause A., Zhu L., Neumayer N., van de Ven G., de Zeeuw P. T., Schödel R., 2017, MNRAS, 466, 4040
Ferré-Mateu A., Trujillo I., Martín-Navarro I., Vazdekis A., Mezcua M., Balcells M., Domínguez L., 2017, MNRAS, 467, 1929
Feruglio C., Maiolino R., Piconcelli E., Menci N., Aussel H., Lamastra A., Fiore F., 2010, A&A, 518, L155
Fluetsch A. et al., 2019, MNRAS, 483, 4586
Foreman-Mackey D., Hogg D. W., Lang D., Goodman J., 2013, PASP, 125, 306
Forrest B. et al., 2020, ApJ, 890, L1
Forrest B. et al., 2025, preprint (arXiv:2508.10987)
Förster Schreiber N. M., Wuyts S., 2020, ARA&A, 58, 661
Förster Schreiber N. M. et al., 2018, ApJS, 238, 21
Fraternali F., Karim A., Magnelli B., Gómez-Guijarro C., Jiménez-Andrade E. F., Posses A. C., 2021, A&A, 647, A194
Fuentealba-Fuentes M., Lira P., Díaz-Santos T., Trakhtenbrot B., Netzer H., Videla L., 2024, A&A, 687, A62

Gardner J. P. et al., 2023, PASP, 135, 068001
Genzel R. et al., 2020, ApJ, 902, 98
Gilli R. et al., 2014, A&A, 562, A67
Glazebrook K. et al., 2017, Nature, 544, 71
Glazebrook K. et al., 2024, Nature, 628, 277
Goodman J., Weare J., 2010, Commun. Appl. Math. Comput. Sci., 5, 65
Graham M. T. et al., 2018, MNRAS, 477, 4711
Gunn J. E., Gott J. R., III, 1972, ApJ, 176, 1
Harborne K. E., van de Sande J., Cortese L., Power C., Robotham A. S. G., Lagos C. D. P., Croom S., 2020, MNRAS, 497, 2018
Harrison C. M., Costa T., Tadhunter C. N., Flütsch A., Kakkad D., Perna M., Vietri G., 2018, Nat. Astron., 2, 198
Hartley A. I. et al., 2023, MNRAS, 522, 3138
Hartmann E. A., Martín-Navarro I., Huertas-Company M., Benedetti J. P. V., Iglesias-Navarro P., Vazdekis A., Montes M., 2025, A&A, 694, L7
Hilz M., Naab T., Ostriker J. P., Thomas J., Burkert A., Jesseit R., 2012, MNRAS, 425, 3119
Hilz M., Naab T., Ostriker J. P., 2013, MNRAS, 429, 2924
Hopkins P. F., Hernquist L., Cox T. J., Kereš D., 2008, ApJS, 175, 356
van Houdt J. et al., 2021, ApJ, 923, 11
Ikarashi S., Ivison R. J., Cowley W. I., Kohno K., 2022, A&A, 659, A154
Ito K. et al., 2024, ApJ, 964, 192
Jakobsen P. et al., 2022, A&A, 661, A80
Jarvis M. J. et al., 2013, MNRAS, 428, 1281
Ji Z. et al., 2024a, preprint (arXiv:2401.00934)
Ji Z. et al., 2024b, preprint (arXiv:2409.17233)
Ji Z. et al., 2024c, ApJ, 974, 135
Jin Y., Zhu L., Long R. J., Mao S., Xu D., Li H., van de Ven G., 2019, MNRAS, 486, 4753
Kawinwanichakij L. et al., 2026, ApJ, 997, 29
Kereš D., Katz N., Weinberg D. H., Davé R., 2005, MNRAS, 363, 2
Kimmig L. C., Remus R.-S., Seidel B., Valenzuela L. M., Dolag K., Burkert A., 2025, ApJ, 979, 15
Klypin A. A., Trujillo-Gomez S., Primack J., 2011, ApJ, 740, 102
Kroupa P., 2001, MNRAS, 322, 231
Kuhn L. et al., 2024, A&A, 684, A52
Lablanche P.-Y. et al., 2012, MNRAS, 424, 1495
Lagos C. D. P., Cora S. A., Padilla N. D., 2008, MNRAS, 388, 587
Lagos C. d. P. et al., 2015, MNRAS, 452, 3815
Lagos C. d. P. et al., 2018, MNRAS, 473, 4956
Lagos C. d. P., Emsellem E., van de Sande J., Harborne K. E., Cortese L., Davison T., Foster C., Wright R. J., 2022, MNRAS, 509, 4372
Lagos C. d. P. et al., 2024, MNRAS, 531, 3551
Lagos C. d. P. et al., 2025, MNRAS, 536, 2324
Leung G. Y. C. et al., 2018, MNRAS, 477, 254
Lim S., Tacchella S., Maiolino R., Schaye J., Schaller M., 2025, MNRAS, 543, 2204
Long A. S. et al., 2024, ApJ, 970, 68
Lorenzon G. et al., 2025, A&A, 693, A118
Lovell C. C. et al., 2023, MNRAS, 525, 5520
Lu S., Zhu K., Cappellari M., Li R., Mao S., Xu D., 2024, MNRAS, 530, 4474
Ludlow A. D., Schaye J., Bower R., 2019, MNRAS, 488, 3663
Maiolino R. et al., 2012, MNRAS, 425, L66
Maksymowicz-Maciata M. et al., 2024, MNRAS, 531, 2864
Man A., Belli S., 2018, Nat. Astron., 2, 695
McClymont W. et al., 2025, MNRAS, 544, 1732
McDermid R. M. et al., 2015, MNRAS, 448, 3484
McLeod D. J., McLure R. J., Dunlop J. S., Cullen F., Carnall A. C., Duncan K., 2021, MNRAS, 503, 4413
Mendel J. T. et al., 2020, ApJ, 899, 87
Metropolis N., Rosenbluth A. W., Rosenbluth M. N., Teller A. H., Teller E., 1953, J. Chem. Phys., 21, 1087
Nanayakkara T. et al., 2024, Scientific Rep., 14, 3724
Nanayakkara T. et al., 2025, ApJ, 981, 78
Navarro J. F., Frenk C. S., White S. D. M., 1996, ApJ, 462, 563
Nelson D. et al., 2019, Comput. Astrophys. Cosmol., 6, 2
Newman A. B., Belli S., Ellis R. S., Patel S. G., 2018a, ApJ, 862, 125
Newman A. B., Belli S., Ellis R. S., Patel S. G., 2018b, ApJ, 862, 126
Newman A. B. et al., 2025, preprint (arXiv:2503.17478)
Nipoti C., Treu T., Bolton A. S., 2009, ApJ, 703, 1531
Park M. et al., 2024, ApJ, 976, 72
Parlanti E., Carniani S., Pallottini A., Cignoni M., Cresci G., Kohandel M., Mannucci F., Marconi A., 2023, A&A, 673, A153
Pasha I., Miller T. B., 2023, J. Open Source Softw., 8, 5703
Peng Y. et al., 2015, Nature, 521, 192
Pérez-González P. G. et al., 2025, Nat. Astron., 9, 1240
Perna M. et al., 2023, A&A, 679, A89
Pillepich A. et al., 2018, MNRAS, 473, 4077
Piotrowska J. M., Bluck A. F. L., Maiolino R., Peng Y., 2022, MNRAS, 512, 1052
Planck Collaboration VI, 2020, A&A, 641, A6
Puskás D. et al., 2025, MNRAS, 540, 2146
Rauscher B. J. et al., 2017, PASP, 129, 105003
Remus R.-S., Kimmig L. C., 2025, ApJ, 982, 30
Riechers D. A. et al., 2020, ApJ, 895, 81
Rieke M. J. et al., 2023, ApJS, 269, 16
Rigby J. et al., 2023, PASP, 135, 048001
Rizzo F., Vegetti S., Powell D., Fraternali F., McKean J. P., Stacey H. R., White S. D. M., 2020, Nature, 584, 201
Rizzo F., Vegetti S., Fraternali F., Stacey H. R., Powell D., 2021, MNRAS, 507, 3952
Rowlands K., Wild V., Nesvadba N., Sibthorpe B., Mortier A., Lehnert M., da Cunha E., 2015, MNRAS, 448, 258
Sales L. V., Navarro J. F., Theuns T., Schaye J., White S. D. M., Frenk C. S., Crain R. A., Dalla Vecchia C., 2012, MNRAS, 423, 1544
Salpeter E. E., 1955, ApJ, 121, 161
Sánchez-Blázquez P. et al., 2006, MNRAS, 371, 703
Schaye J. et al., 2015, MNRAS, 446, 521
Schaye J. et al., 2023, MNRAS, 526, 4978
Schaye J. et al., 2025, preprint (arXiv:2508.21126)
Scholtz J. et al., 2024, preprint (arXiv:2405.19401)
Schulze F., Remus R.-S., Dolag K., Burkert A., Emsellem E., van de Ven G., 2018, MNRAS, 480, 4636
Schwarzschild M., 1979, ApJ, 232, 236
Sersic J. L., 1968, Atlas de Galaxias Australes
Setton D. J. et al., 2024, ApJ, 974, 145
Sharda P. et al., 2019, MNRAS, 487, 4305
Shetty S., Cappellari M., 2015, MNRAS, 454, 1332
Silk J., Rees M. J., 1998, A&A, 331, L1
Sillassen N. B. et al., 2025, A&A, 693, A309
Simons R. C. et al., 2016, ApJ, 830, 14
Slob M. et al., 2025, A&A, 702, A110
Somerville R. S., Davé R., 2015, ARA&A, 53, 51
Springel V. et al., 2018, MNRAS, 475, 676
Suess K. A., Kriek M., Price S. H., Barro G., 2021, ApJ, 915, 87
Suess K. A. et al., 2023, ApJ, 956, L42
Sun F. et al., 2024, ApJ, 961, 69
Suzuki T. L. et al., 2022, ApJ, 936, 61
Tacchella S. et al., 2015, Science, 348, 314
Tacchella S., Dekel A., Carollo C. M., Ceverino D., DeGraf C., Lapiner S., Mandelker N., Primack Joel R., 2016, MNRAS, 457, 2790
Tacchella S., Bose S., Conroy C., Eisenstein D. J., Johnson B. D., 2018, ApJ, 868, 92
Tacchella S. et al., 2019, MNRAS, 487, 5416
Tacchella S. et al., 2022, ApJ, 926, 134
Tan Q. et al., 2014, A&A, 569, A98
Thob A. C. R. et al., 2019, MNRAS, 485, 972
Thomas D., Maraston C., Schawinski K., Sarzi M., Silk J., 2010, MNRAS, 404, 1775
Toft S. et al., 2017, Nature, 546, 510
Trujillo I., Ferré-Mateu A., Balcells M., Vazdekis A., Sánchez-Blázquez P., 2014, ApJ, 780, L20
Turner C. et al., 2025, MNRAS, 537, 1826
Valentino F. et al., 2023, ApJ, 947, 20
van der Marel R. P., van Dokkum P. G., 2007, ApJ, 668, 738

van de Sande J. et al., 2017, MNRAS, 472, 1272
van de Sande J. et al., 2018, Nat. Astron., 2, 483
van de Ven G., van der Wel A., 2021, ApJ, 914, 45
van de Ven G., Falcón-Barroso J., McDermid R. M., Cappellari M., Miller B. W., de Zeeuw P. T., 2010, ApJ, 719, 1481
van der Wel A. et al., 2016, ApJS, 223, 29
van der Wel A. et al., 2022, ApJ, 936, 9
Vani A., Ayromlou M., Kauffmann G., Springel V., 2025, MNRAS, 536, 777
Veale M. et al., 2017a, MNRAS, 464, 356
Veale M., Ma C.-P., Greene J. E., Thomas J., Blakeslee J. P., McConnell N., Walsh J. L., Ito J., 2017b, MNRAS, 471, 1428
Veilleux S. et al., 2020, A&AR, 28, 2
Weibel A. et al., 2025, ApJ, 983, 11
Westfall K. B. et al., 2019, AJ, 158, 231
Whitaker K. E. et al., 2021, Nature, 597, 485
White S. D. M., Rees M. J., 1978, MNRAS, 183, 341
Williams C. C. et al., 2021, ApJ, 908, 54
Willmer C. N. A., 2018, ApJS, 236, 47
Wisnioski E. et al., 2015, ApJ, 799, 209
Wisnioski E. et al., 2019, ApJ, 886, 124
Woodrum C. et al., 2022, ApJ, 940, 39
Wright L. et al., 2024, ApJ, 964, L10
Wyithe J. S. B., Turner E. L., Spergel D. N., 2001, ApJ, 555, 504
Xie L. et al., 2024, ApJ, 966, L2
Zhang T.-Z., Wu X.-B., 2002, Chin. J. Astron. Astrophys., 2, 487
Zhang Y. et al., 2026, ApJ, 997, 252
Zhu K., Lu S., Cappellari M., Li R., Mao S., Gao L., 2023, MNRAS, 522, 6326
Zhu Y. et al., 2024, Res. Notes Am. Astron. Soc., 8, 284
Zolotov A. et al., 2015, MNRAS, 450, 2327

APPENDIX A: BEST-FITTING PARAMETERS FROM PYSERSIC PHOTOMETRY FITTING

These tables present the best-fitting parameters that we obtain from PySersic photometry fitting of the galaxy image in NIRCam's *F*200*W* filter. The first table gives the parameters obtained using the Laplace sampling method of retrieving the best-fitting parameters from the chains' samples. In general, the SVI flow method is more reliable and accurate so we chose to use these values in our subsequent analysis. For the data reported in Table A1, we use a prior assumption of a simple Sérsic profile across all the galaxy.

Table A1. Best-ftting parameters for PySersic*F*200*W* Image-Laplace sampling method.

Parameter	Value
Observed ellipticity	0.252 ± 0.015
Sérsic index	2.958 ± 0.140
$R_{\rm eff}$ (arcsec)	0.0345 ± 0.0007
θ (deg)	174.3 ± 7.0

APPENDIX B: JAM DYNAMICAL MODEL TEST FOR THE CENTRAL BLACK HOLE MASS

This alternative dynamical model (*Alternative-1*) is a simple mass-follows-light (MFL) model (i.e. no dark matter component) with an additional central BH mass ($M_{\rm BH}$). As we can remark from Fig. B1, we cannot pose tight constraints on $M_{\rm BH}$ but we are able to reject central black holes with masses $\rm M_{BH} > 10^{9.27}\ M_\odot$ at 2σ level (97.7 per cent) and $M_{\rm BH} > 10^{9.76}\ \rm M_\odot$ at 3σ level (99.9 per cent).

Using $\rm M_{BH} = 10^{8.8}\ M_\odot$ and $\sigma'_* = 239\ \rm km\,s^{-1}$, the radius of the sphere of influence of the black hole is about $R_{\rm i,BH} = \rm GM_{BH}/\sigma'^2_* = 50\ pc \equiv 7.7$ mas, 6.5 times below the pixel resolution of our IFU data (0.05 arcsec). This angular resolution limitation is the main reason for which we can only infer an upper black hole mass for GS-9209. The inferred stellar mass is $\log(\rm M_*/M_\odot) = 10.61 \pm 0.03$, in remarkable agreement with the value obtained from the *Fiducial* dynamical model (see Section 4.2).

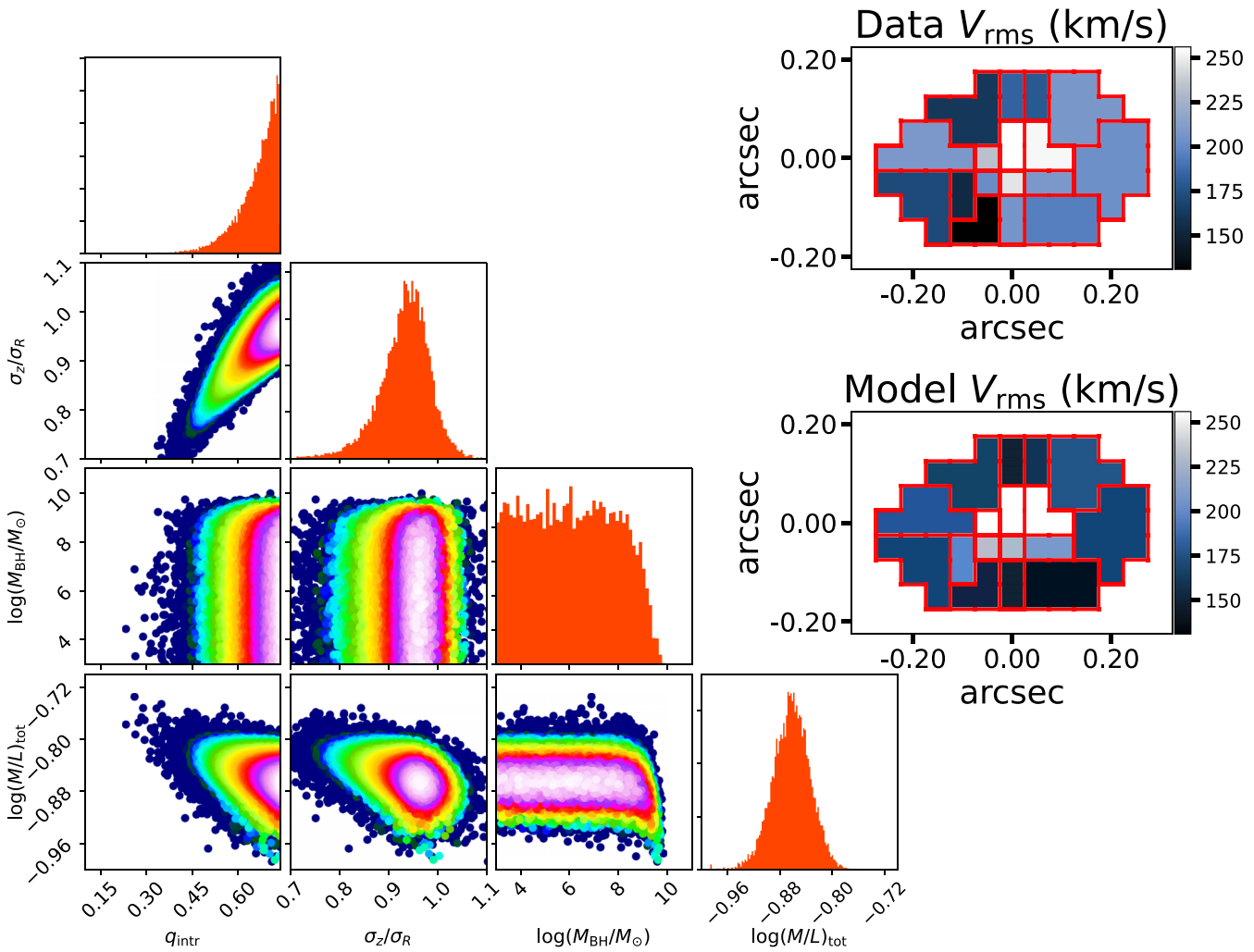

Figure B1. Outputs of the model *Alternative-1*, assuming that we only have a central BH, which, together with the stellar mass itself, are responsible for producing the gravitational potential (hence the stellar kinematics). Because the galaxy is quiescent, we can safely neglect the mass of interstellar gas (and dust). This is a Black-Hole & Mass-Follows-Light (BH + MFL) model. The best-fitting parameters predicted by this model are given in Table B1. The two panels on the right-hand side show the input versus the output map of $V_{\rm rms}$ predicted by this model. In this plot we denote $\log(M/L)_{\rm tot} \equiv \log[(M/L)_{\rm tot}/(\mathrm{M}_\odot/L_\odot)]$. This model has reduced $\chi^2_r = 2.7$.

Table B1. Marginalized posterior probabilities on the free parameters of the *Alternative-1* model (BH allowed to be fit freely and mass follows light). The values reported are the median and 16th–84th percentile probability range.

Parameter	Value	Model
$q_{\rm intr}$	0.67 ± 0.06	*Alternative-1*
σ_z/σ_R	0.94 ± 0.05	*Alternative-1*
$\log M_{\rm BH}/\mathrm{M}_\odot$	$< 9.27\,(2\sigma)$	*Alternative-1*
$\log[(M/L)_{\rm tot}/(\mathrm{M}_\odot/L_\odot)]$	-0.91 ± 0.03	*Alternative-1*

APPENDIX C: JAM DYNAMICAL MODEL TEST WITH TANGENTIAL ANISOTROPY σ_ϕ/σ_R

In this case, we use a dynamical model similar to our *Fiducial* model: classical NFW Dark Matter Halo density profile, but this time we fit V_* instead of $V_{\rm rms}$. We adopt Gaussian priors on all the parameters to be fitted, as explain in the caption of Fig. C1. As this figure shows, *Alternative-2* dynamical model constrains the tangential anisotropy to be $\sigma_\phi/\sigma_{\rm R} = 1.01 \pm 0.05$. This quantity is important because it is used in de-projection calculations.

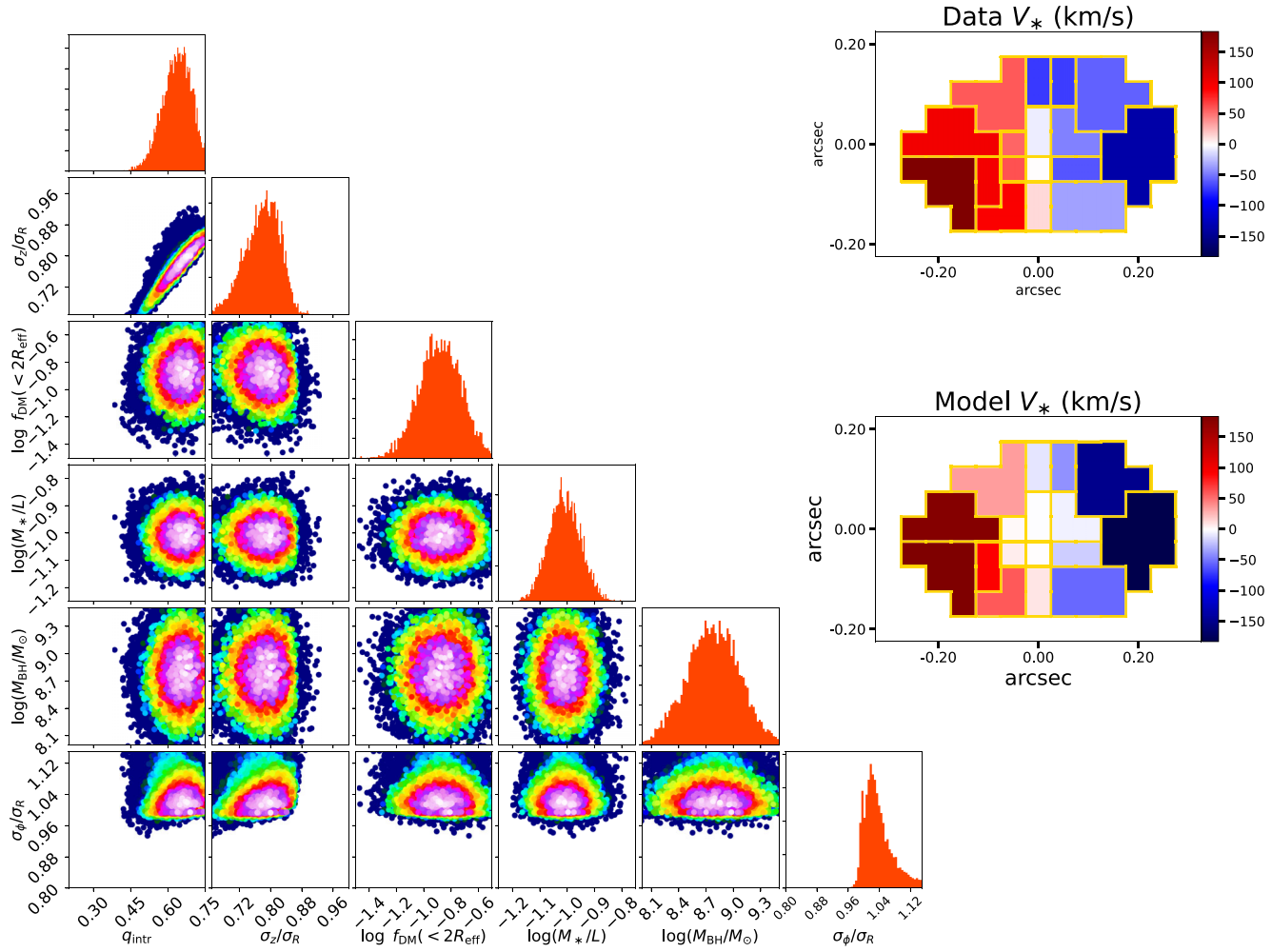

Figure C1. This figure shows the dynamical model *Alternative-2*, which fits the first LOSVD moment of the stellar kinematics, V_*. This model has similar characteristics to the *Fiducial* model except that now we allow for a tangential anisotropy σ_ϕ/σ_R (with a Gaussian prior of mean = 1, standard deviation = 0.2, this choice being motivated by the second panel of fig. 2 from M. Cappellari et al. 2007). We also impose Gaussian priors on the other five parameters, as follows: $q_{\rm intr}$ (mean: 0.62, standard deviation: 0.10), $\sigma_{\rm z}/\sigma_{\rm R}$ (mean: 0.846, standard deviation: 0.08), $\log f_{\rm DM}\,(<2R_{\rm eff})$ (mean: −0.84, standard deviation: 0.16), $\log[(M_*/L)/(\rm M_\odot/L_\odot)]$ (mean: −1.01, standard deviation: 0.06), $\log(M_{\rm BH}/\rm M_\odot)$ (mean: 8.8, standard deviation: 0.3). These priors are motivated by the output results of the *Fiducial* dynamical model. In this plot, we denote $\log(M_*/L) \equiv \log[(M_*/L)/(\rm M_\odot/L_\odot)]$.

Table C1. Best-fitting parameters and uncertainties from *JAM* using the dynamical model *Alternative-2* (tangential anisotropy, NFW DM density profile). The Gaussian priors on each parameter are given in the caption of Fig. C1.

Parameter	Best-fitting value
$q_{\rm intr}$	0.64 ± 0.06
σ_z/σ_R	0.79 ± 0.05
$\log f_{\rm DM}\,(<2R_{\rm eff})$	-0.88 ± 0.16
$\log\left[(M_*/L)/(\rm M_\odot/L_\odot)\right]$	-1.01 ± 0.06
σ_ϕ/σ_R	1.01 ± 0.05
$\log(M_{\rm BH}/\rm M_\odot)$	8.85 ± 0.29

APPENDIX D: JAM DYNAMICAL MODEL TEST WITH A GAUSSIAN PRIOR ON THE INTRINSIC AXIAL RATIO

This dynamical model fits $V_{\rm rms}$ and it is similar to the *Fiducial* model, the only difference being the fact that now we introduce a Gaussian prior on $q_{\rm intr}$ (in addition to the already existing prior on the central BH mass). The reason for this test is to probe to what extent the predictions on $q_{\rm intr}$ that are purely based on our data alone can win against a physically motivated prior. The results of *Alternative-3* dynamical model fitting are given in Table D1.

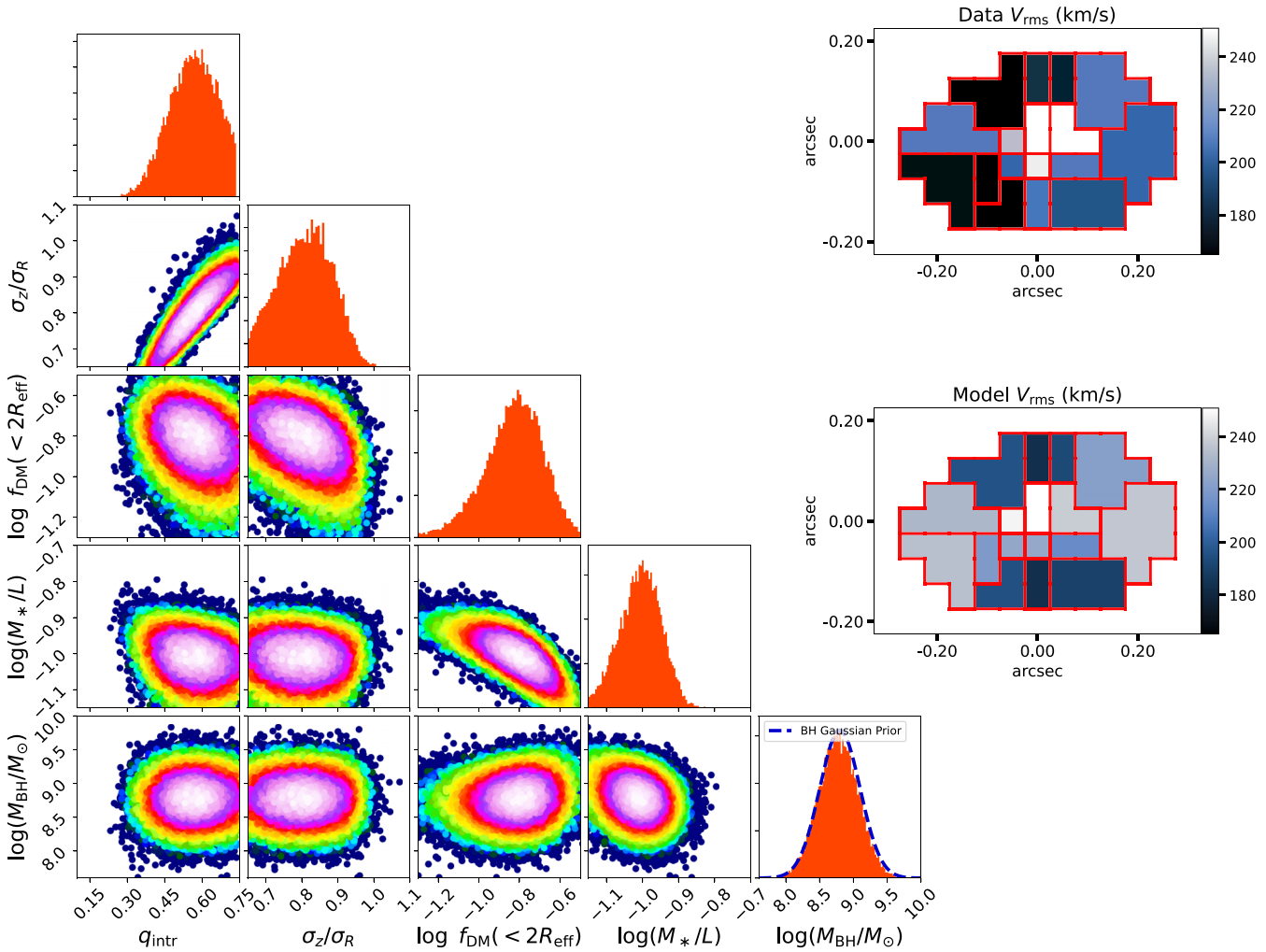

Figure D1. This figure shows the dynamical model *Alternative-3*, which has similar characteristics to *Fiducial* except that now we force a Gaussian prior on $q_{\rm intr}$ (mean = 0.41, standard deviation = 0.18) allowing σ_z/σ_R, log $f_{\rm DM}(<2R_{\rm eff})$ and $\log[(M_*/L)/(\mathrm{M}_\odot/L_\odot)]$ as free parameters. In this plot, we denote $\log(M_*/L) \equiv \log[(M_*/L)/(\mathrm{M}_\odot/L_\odot)]$. This model has a reduced $\chi^2_{\rm r} = 1.65$, which is larger than $\chi^2_{\rm r} = 1.4$ of the *Fiducial* dynamical model.

Table D1. Best-fitting parameters from *JAM* using the dynamical model *Alternative-3* (NFW DM density profile, Gaussians priors on $q_{\rm intr}$ and $\log M_{\rm BH}$). The Gaussian priors on each parameter are given in the caption of Fig. D1.

Parameter	Best-fitting value
$q_{\rm intr}$	0.57 ± 0.09
σ_z/σ_R	0.81 ± 0.09
$\log f_{\rm DM}(<2R_{\rm eff})$	-0.82 ± 0.14
$\log\left[(M_*/L)/(\mathrm{M}_\odot/L_\odot)\right]$	-1.01 ± 0.06
$\log\left(M_{\rm BH/M_\odot}\right)$	8.79 ± 0.29

APPENDIX E: DARK MATTER CONTENT-COMPARISON WITH THE TNG-50 SIMULATIONS

Based on their study of *EAGLE* hydrodynamical simulations (J. Schaye et al. 2015), A. D. Ludlow, J. Schaye & R. Bower (2019) propose the following criterion for simulated galaxies size convergence:

$$R_{\rm gal} \geq R_{\rm conv} \equiv 0.055\,\mathrm{L}\,(\mathrm{z}), \tag{E1}$$

with $L\,(\mathrm{z})$ being the mean spacing between dark matter particles, calculated using the equation $L\,(\mathrm{z}=0) = L_{\rm box}/N_{\rm DM}^{1/3}$ and $L\,(z) = L\,(\mathrm{z}=0)/(1+z)$. The values for the threshold convergence radius for a number of *TNG* simulation boxes (D. Nelson et al. 2019), as well as for the *EAGLE* (J. Schaye et al. 2015), *Illustris-1* (A. Pillepich et al. 2018; V. Springel et al. 2018), *SIMBA* (R. Davé et al. 2019), *FLAMINGO* (J. Schaye et al. 2023), *Magneticum* (R.-S. Remus & L. C. Kimmig 2025), and COLIBRE (J. Schaye et al. 2025) cosmological simulations, are given in Table E1. For GS-9209, the effective light radius is $R_{\rm eff} \approx 223 \pm 20$ pc, which is below the convergence radius calculated using this criterion, for all simulations considered except for *TNG50-1* (which has a convergence radius comparable to GS-9209 effective radius). This means that all the other simulations cannot accurately probe the existence and number densities of extremely compact high-redshift MQGs, because the size convergence is uncertain for simulated galaxies that have $R_{\rm eff} < R_{\rm conv}$. We will therefore focus on analysing the MQGs produced within the *TNG50-1* simulation box.

We compare $f_{\rm DM}(<2R_{\rm eff})$ of GS-9209 with the values in the cases of simulated galaxies in the *TNG50-1* box. However, these simulations compute the dark matter fraction within twice the

Table E1. Convergence radii (using the criterion from A. D. Ludlow et al. 2019) for various simulations that we considered for analysing their predictions for the dark matter content of GS-9209 at $z = 4.66$. This table justifies our choice of TNG50-1 in our analysis: this box has a similar spatial resolution to GS-9209 effective radius and the box size is still reasonably large (50 cMpc h^{-1}) to probe a reasonable cosmic volume at $z = 4.66$.

Simulation box	R_{conv} (pc)
TNG50-1	233
TNG100-1	591
ILLUSTRIS-1	568
EAGLE-100 cMpc box	646
EAGLE-25 cMpc box	323
MAGNETICUM-uhr resolution	1195
MAGNETICUM-xhr resolution	447
COLIBRE-L050m5 box	301
COLIBRE-L200m6 box	601
SIMBA	1406
FLAMINGO-best resolution	2700

stellar half mass radius $2R_{eff,M,*}$ (twice the radius enclosing half of the total stellar mass within a given subhalo). PYSERSIC computed the projected effective light radius obtained from the galaxy's photometry data in NIRCam/*F*200*W* band, $R_{eff,2D}$. The first step is to use *JAM* dynamical modelling to compute the three-dimensional intrinsic half light radius $R_{eff,lum,3D}$ (the radius of a sphere enclosing half of the total light emitted over the entire volume of the galaxy) of GS-9209. This is done by using an entirely analogous procedure to JAM_MGE_HALF_LIGHT_RADIUS. The latter computes the radius of a circle enclosing half of the light within the surface brightness Gaussian surfaces (characterized by I_j, σ_j, and q'_j using the same notations as in Section 3.1.2) from the *MGE* parametrization of the galaxy's Sérsic profile fitted by PYSERSIC to the original image. Instead, we need to convert these surface brightness Gaussians to luminosity density Gaussians as we did in Section 4.4.4. The intrinsic luminosity density Gaussians are characterized by ν_j, σ_j, and q_j (with the same notations as in equation 14). The integrated luminosity of a Gaussian is given by (equation 13 from M. Cappellari 2008):

$$L_j = \nu_j q_j \times \left(\sigma_j \sqrt{2\pi}\right)^3. \quad \text{(E2)}$$

The total luminosity of all the Gaussians is the sum of L_j values. This allows us to compute the radial distance at which Gaussians within that aperture only add up to half the total luminosity. We obtain that, for GS-9209, $R_{eff,lum,3D} = 0.91\ R_{eff,2D}$, where $R_{eff,2D}$ is the effective light radius from the *F*200*W* image. This is in good agreement with the findings highlighted in the top-left panel of fig. 4 from G. de Ven & A. van der Wel (2021) who determine similar values for the ratio between the two-dimensional projected effective light radius and the three-dimensional intrinsic counterpart. Because GS-9209 is an MQG, it is reasonable to assume that its gas mass is negligible. Future studies using the G395H/F270LP spectrum from NIRSpec will allow us to quantify neutral gas in the galaxy's interstellar medium, whereas ALMA could determine the amount of cold gas (or at least impose a stringent upper limit for the cold gas mass in GS-9209). Studies such as J. Scholtz et al. (2024) showed that for GS-10578, an MQG at $z \sim 3$, the CO-derived cold gas mass is less than 3 per cent of its M_*, whereas F. D'Eugenio et al. (2024) determine that the neutral gas mass of GS-10578 is about 10^8 $M_\odot$ (derived from NaD absorption). The upper limits found by T. L. Suzuki et al. (2022) on the gas fractions of five

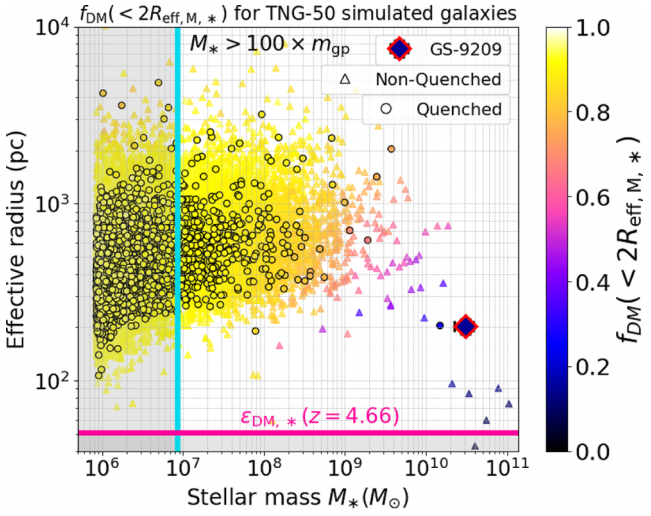

Figure E1. Dark matter fraction within 2 $R_{eff,M,*}$ of simulated galaxies at $z \sim 4.66$ in *TNG50-1* run. We observe that as we go towards smaller effective radii and larger stellar masses, f_{DM} decreases. There is good agreement between the value obtained from our *JAM* dynamical modelling algorithm $f_{DM}\left(<2R_{eff,M,*}\right) = 14.5^{+6.0}_{-4.2}$ per cent and the predictions given by the *TNG-50* simulation. We remark a similar behaviour for the variation of $f_{DM}\left(<2R_{eff,M,*}\right)$ across the mass–size plane for the quiescent versus non-quiescent simulated galaxies. The quiescence criterion is sSFR $< 0.2/t_H\,(z = 4.66)$. The vertical line is the threshold below which the stellar masses of the simulated galaxies are smaller than $100 \times m_{gp}$ (where m_{gp} is the mass of a gas particle). The horizontal line is the physical Plummer-equivalent gravitational softening parameter $\epsilon_{DM,*}(z = 4.66)$ (for collisionless particles i.e. dark matter and stars). This is calculated as $\epsilon_{DM,*}(z) = \epsilon^{z=0}_{DM,*}/(1+z)$ with $\epsilon^{z=0}_{DM,*} = 290$ pc for *TNG50-1*. The plotted simulations data were smoothed using the two-dimensional Locally-Weighted Regression (*LOESS*; W. S. Cleveland & S. J. Devlin 1988) to ensure that each data point shows the local average trend and to remove local outliers.

MQGs at $3.5 < z < 4$ and with $10.5 < \log(M_*/M_\odot) < 11.0$ are less stringent ($f_{gas} \leq 20$ per cent) but consistent with the general picture that high-redshift MQGs are highly likely to contain very little cold gas. For these reasons, we can consider that stars are the only luminous component in our model of GS-9209. Assuming no spatial variation of the stellar mass-to-light ratio, it means that $R_{eff,lum,3D} = R_{eff,M,*} = 0.91\ R_{eff} = 203$ pc. This result is in agreement with the findings from fig. 8 of A. Graaff et al. (2022) based on $z \sim 0.1$ galaxies from *EAGLE* simulations, who obtain that for the most compact galaxies in their sample, their photometry-based effective radii are typically slightly larger than the mass effective radii, but the difference is less than 0.1 dex.

In order to compute f_{DM} within 2 $R_{eff,M,*}$ we use the method outlined below. We chose the snapshot that is closest to the redshift of GS-9209, which has the ID '18' and redshift $z_{snap} \approx 4.66$. We use the provided group catalogues to extract all the galaxy or halo properties needed in the subsequent analysis. Specifically, all the quantities we need at this point reside in the *Subhalos* data repositories (these are retrieved using the *Subfind* algorithm modified to account for the properties and behaviour of the galaxies' baryonic component). For our analysis we only need the quantities that can be queried using the keywords: SUBHALOMASSINRADTYPE, SUBHALOHALFMASSRADTYPE, SUBHALOMASSTYPE, and SUBHALOSFR. SUBHALOFLAG is used to eliminate possible artefacts from our sample. This is particularly important for our analysis because such contaminating subhaloes are

typically compact and baryon dominated (although usually more than three orders of magnitude less massive than GS-9209). They are not individual galaxies but clumps within genuine galaxies. The first keyword is used to extract, from the group catalogue, the masses for each component of a galaxy (gas, DM, stars + winds, BH) within 2 $R_{\rm eff,M,*}$, and hence to compute the DM fraction within this aperture $f_{\rm DM}\,(<2R_{\rm eff,M,*}) = M_{\rm DM}\,(<2R_{\rm eff,M,*})\,/M_{\rm tot}\,(<2R_{\rm eff,M,*})$. The total mass is obtained by adding up all the particles of all types within $<2R_{\rm eff,M,*}$ from the subhalo's centre of mass. The second keyword gives the stellar half mass radii of the galaxies in each simulation. The units in the catalogue are ckpc $\rm h^{-1}$ so in order to convert to pkpc, we take $h = 0.6774$ (this value is adopted by TNG simulations) and we divide by $(1+z_{\rm snap})$. The SUBHALOMASSTYPE keyword gives the masses of each component of a galaxy that is gravitationally bound to that subhalo. In our case we are only interested in the stellar mass.

The results of $f_{\rm DM}\,(<2\,R_{\rm eff,M,*})$ variation across the M_*-$R_{\rm eff,M,*}$ are shown in Fig. E1. This plot shows that the low dark matter content of GS-9209 is in good agreement with the values obtained in the case of its simulated counterparts. Furthermore, it is expected that we find a low amount of dark matter within two effective stellar half-mass radii for GS-9209 given its extremely compact size. Analysing the plot, we find that the *TNG50-1* simulation cannot reproduce MQGs with similar stellar masses and effective radii to GS-9209 at $z = 4.66$.

Overall, GS-9209 occupies a notably different position on the mass–size plane than the majority of the population of quiescent galaxies in this simulation (marked as circles). By carefully analysing the high-mass and low-effective radius end of the diagram ($M_* > 10^{10}\,\rm M_\odot$; $R_{\rm eff} < 300$ pc), we notice that there is only one compact MQG similar to GS-9209. This object has a slightly higher dark matter fraction of than the value we infer for GS-9209, but it is still unambiguously baryon dominated. This allows us to estimate the number density of compact massive quiescent galaxies (c-MQGs) like GS-9209 (as predicted by simulations): $n_{\rm c-MQG} \sim (50/\rm h\ Mpc)^{-3} = 2.4\times10^{-6}\ Mpc^{-3}$. This is approximately one order of magnitude below the calculated number densities values that were reported in various $z = 3$-5 recent MQGs observational studies (e.g K. Glazebrook et al. 2017; F. Valentino et al. 2023; A. C. Carnall et al. 2023a, 2024; M. Park et al. 2024). This result can be explained in two different ways, one of them being the claim that even highly performant cosmological full hydro-dynamical simulations with the best spatial resolution might be unable to fully capture the physical processes that govern the formation and evolution of c-MQGs in the early Universe. However, it is also likely that these simulations do not accurately reproduce compact galaxies, primarily because of size convergence caveats (for *TNG50-1*, $R_{\rm conv}$ is approximately equal to the effective light radius of GS-9209). Even if *TNG50-1* can theoretically probe the regime of compact MQGs, it still struggles to reproduce the existence of objects similar to GS-9209, highlighting the need for building cosmological simulations that have both a large box volume (≥ 100 cMpc $\rm h^{-1}$) and good enough spatial resolution (<200 pc; as defined based on the convergence criterion of A. D. Ludlow et al. 2019). This would be required in order to test whether the disagreement between the observed number densities of high-z MQGs and the predictions of simulations is an issue related to number statistics and computational limitations of the simulations or, alternatively, if the physical mechanisms implemented need to be revised.

APPENDIX F: JAM RECOVERY TESTS OF GALAXY'S DYNAMICAL PARAMETERS

In this section we present some example recovery tests we conducted on our fiducial dynamical model used in the main text. For each of these runs in particular, we use JAM_AXI_PROJ routine to construct a model galaxy data based on a set of four parameters: the intrinsic axial ratio, $q_{\rm intr}$, radial anisotropy ratio, σ_z/σ_R, the stellar mass to light ratio, $\log[((M/L)_{\rm tot}\,/\,(\rm M_\odot/L_\odot)]$, and the logarithmic dark matter fraction within one effective radius, $\log f_{\rm DM}\,(<2R_{\rm eff})$. We have chosen that in this case we will not use the Gaussian prior on the central BH mass and instead just fix it to $M_{\rm BH} = 10^{8.8}\rm M_\odot$ (for speeding up the computations). We show the corner plots illustrating the posterior distributions (and the correlations among these distributions) of the four aforementioned key structural parameters in Figs F1, F2, F3 and F4. Each figure corresponds to one recovery test that we run. We perform the tests as follows:

(i) We start from the values of the parameters obtained for GS-9209 (Table 2). For each parameter, we run one recovery test.

(ii) We vary only one parameter at a time. For instance, for the $q_{\rm intr}$ recovery test, all the other parameters besides $q_{\rm intr}$ are taken to be the values found in Table 2 (and the BH mass is taken as $10^{8.8}\rm M_\odot$). We then assign an arbitrary value for the parameter we want to test, sufficiently different from the value we had in the case of GS-9209 (e.g. $q_{\rm intr} = 0.3$ in our example case that we described).

(iii) We keep doing one such test per parameter per dynamical model. However we do not test for $M_{\rm BH}$ since this value cannot be constrained given the kinematics resolution we have. We test for all the other parameters instead. For the light distribution map we use the same values as obtained from the MGEFIT in the case of GS-9209. We also use the same distance, same Voronoi bins rotated coordinates, same pixel scale as we did for GS-9209 (as keywords for JAM_AXI_PROJ).

(iv) After initializing the set of parameters for a test, the next thing to do is to build the model galaxy kinematics using JAM_AXI_PROJ routine with no input data or error maps. We add the noise after creating the model galaxy using the same noise map as for GS-9209. We pass all of these to the χ^2JAM minimization routine and we run ADAMET with 10^4 steps (instead of 10^5 as we did in the main text dynamical modelling). This is done in order to illustrate the validity of the recovery tests, of the models we used and to allow the computation of more dynamical models tested in a short time. Nevertheless, even in the case of the original dynamical models, the convergence is reached quickly enough that if we use 10^4 steps in ADAMET instead of 10^5, this does not produce a noticeable difference in terms of the retrieved best-fitting parameters from the posterior distribution.

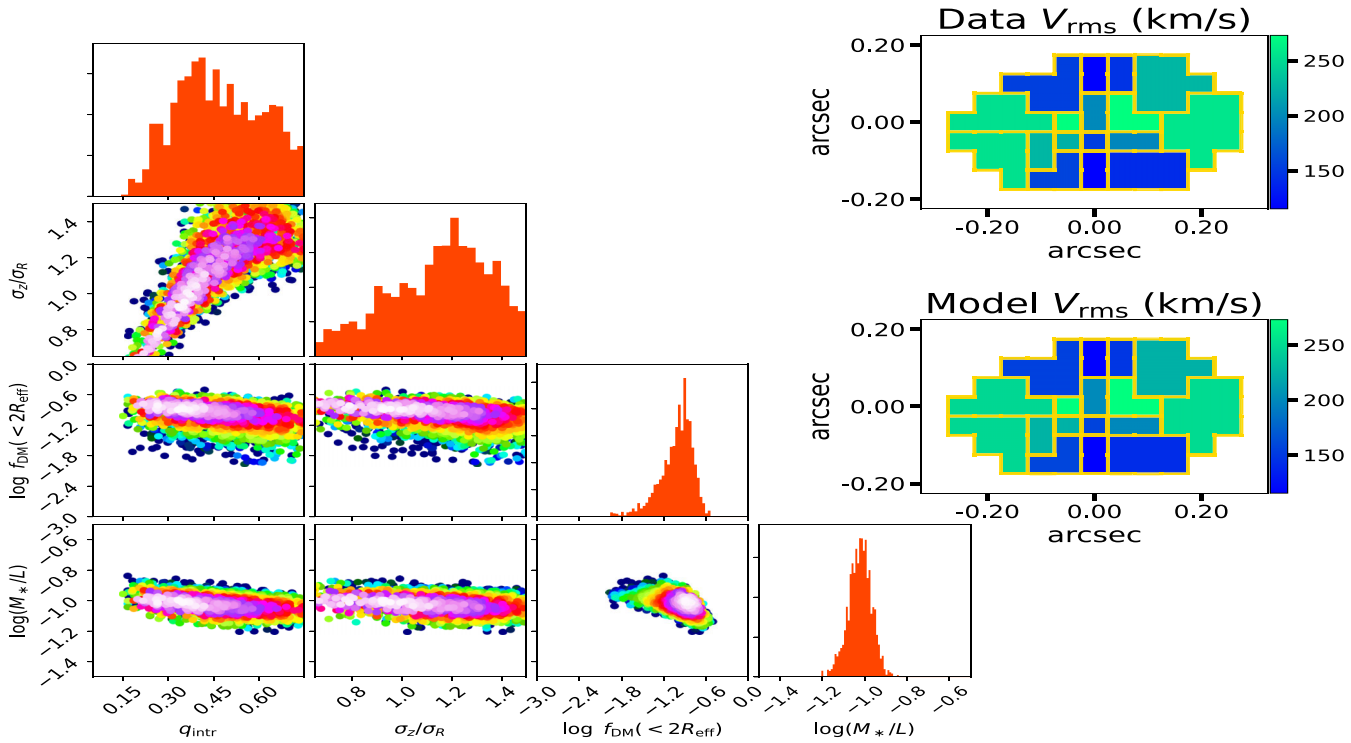

Figure F1. Fiducial recovery test for $q_{\rm intr}$. The tested input value is $q_{\rm test,in} = 0.3$ and the test output is $q_{\rm test,out} = 0.35 \pm 0.12$. We have $(\sigma_z/\sigma_R)_{\rm test,out} = 0.94 \pm 0.22$ (consistent with the input value of 0.85), $\log(M_*/L)_{\rm test,out} = -1.02 \pm 0.05$ (in agreement with the input value of -1.01) and $\left(\log\ f_{\rm DM,<2R_{eff}}\right)_{\rm test,out} = 0.88 \pm 0.22$ (in agreement with the input value of -0.84). In this plot, we denote $\log(M_*/L) \equiv \log\left[(M_*/L)\,/\,(\mathrm{M}_\odot/L_\odot)\right]$.

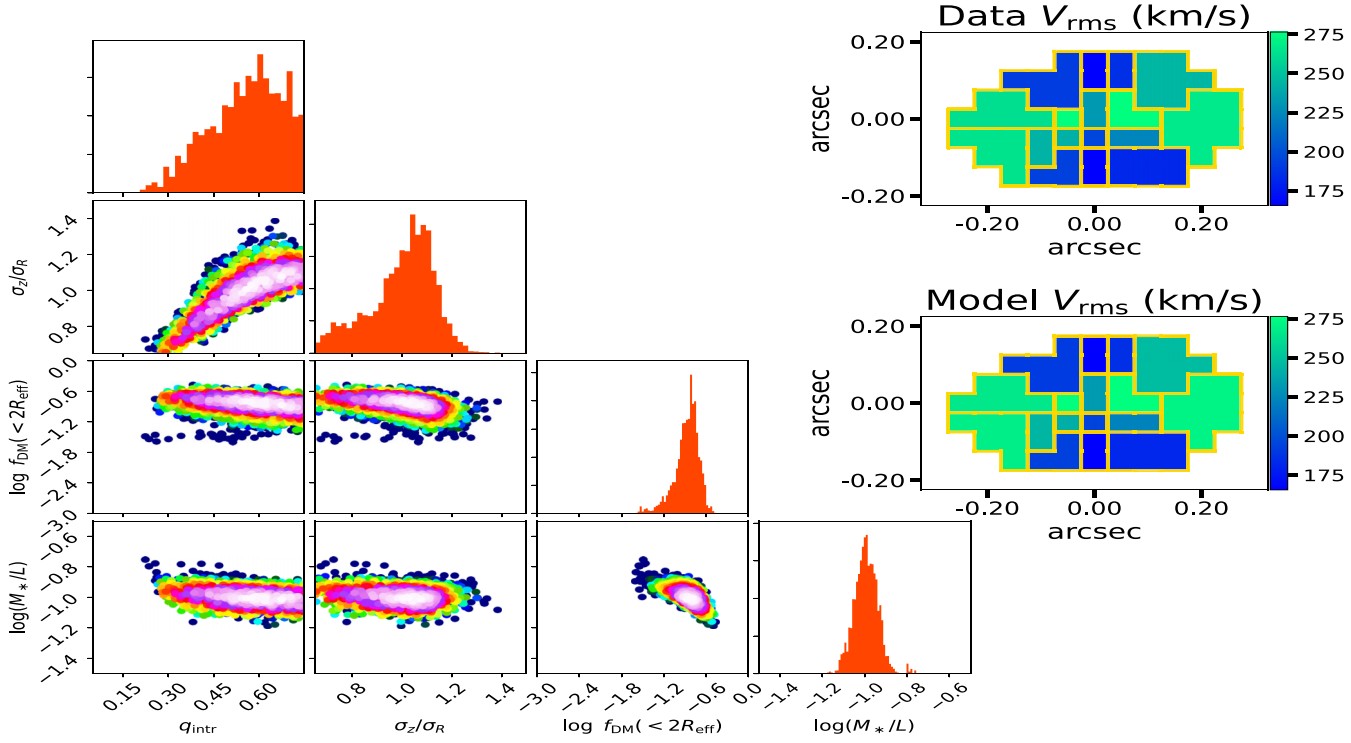

Figure F2. Fiducial recovery test for σ_z/σ_R. The tested input value is $(\sigma_z/\sigma_R)_{\rm test,in} = 1.05$ and the test output is $(\sigma_z/\sigma_R)_{\rm test,out} = 1.00 \pm 0.13$. We have $q_{\rm test,out} = 0.55 \pm 0.13$ (in agreement with the input value of 0.62), $\log(M_*/L)_{\rm test,out} = -1.00 \pm 0.05$ (in agreement with the input value of -1.01), and $\left(\log\ f_{\rm DM,<2R_{eff}}\right)_{\rm test,out} = -0.80 \pm 0.16$ (in agreement with the input value of -0.84). In this plot, we denote $\log(M_*/L) \equiv \log\left[(M_*/L)\,/\,(\mathrm{M}_\odot/L_\odot)\right]$.

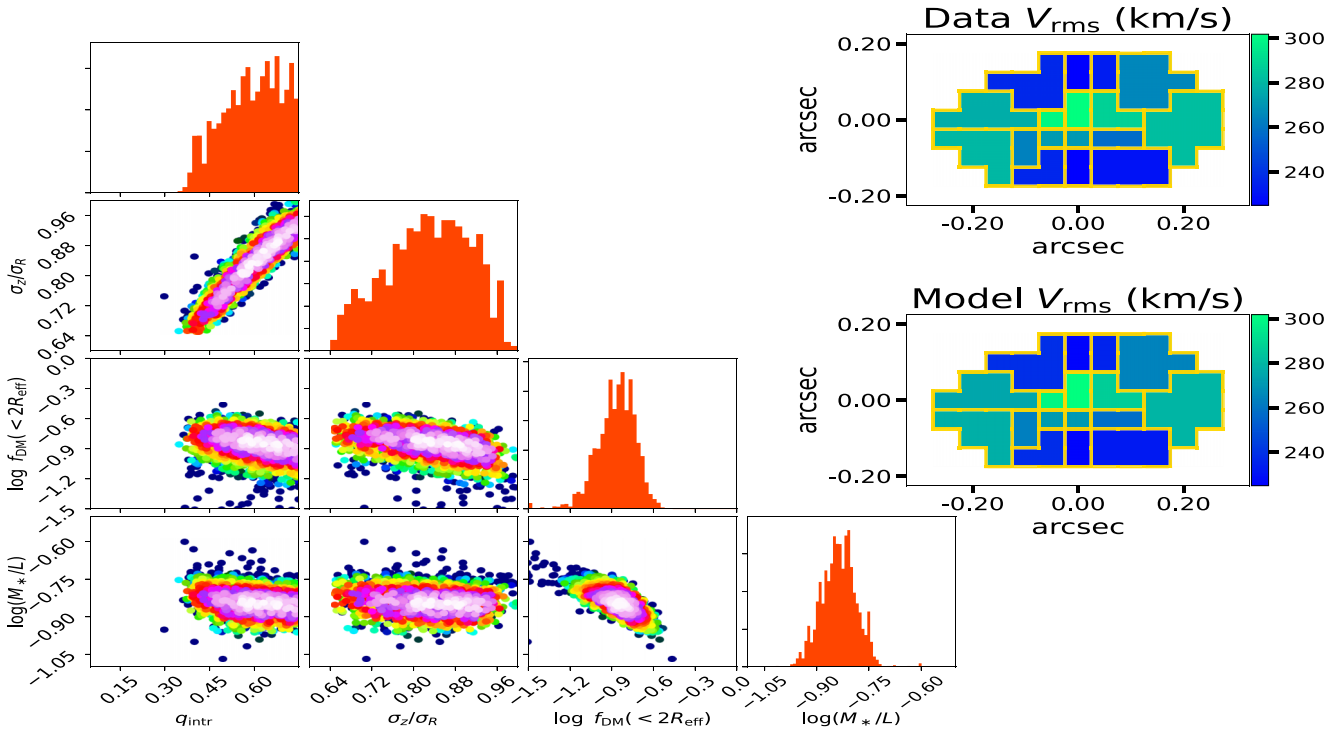

Figure F3. Fiducial recovery test for $\log(M_*/L)$. The tested input value is $\log(M_*/L)_{\rm test,in} = -0.85$ and the test output is $\log(M_*/L)_{\rm test,out} = -0.86 \pm 0.04$. We have $(\sigma_z/\sigma_R)_{\rm test,out} = 0.89 \pm 0.09$ (in agreement with the input value of 0.85), $q_{\rm test,out} = 0.66 \pm 0.11$ (in agreement with the input value of 0.62), and $\log\left(f_{\rm DM,<2R_{eff}}\right)_{\rm test,out} = -0.85 \pm 0.14$ (in agreement with the input value of -0.84). In this plot, we denote $\log(M_*/L) \equiv \log\left[(M_*/L)\,/\,(\mathrm{M}_\odot/L_\odot)\right]$.

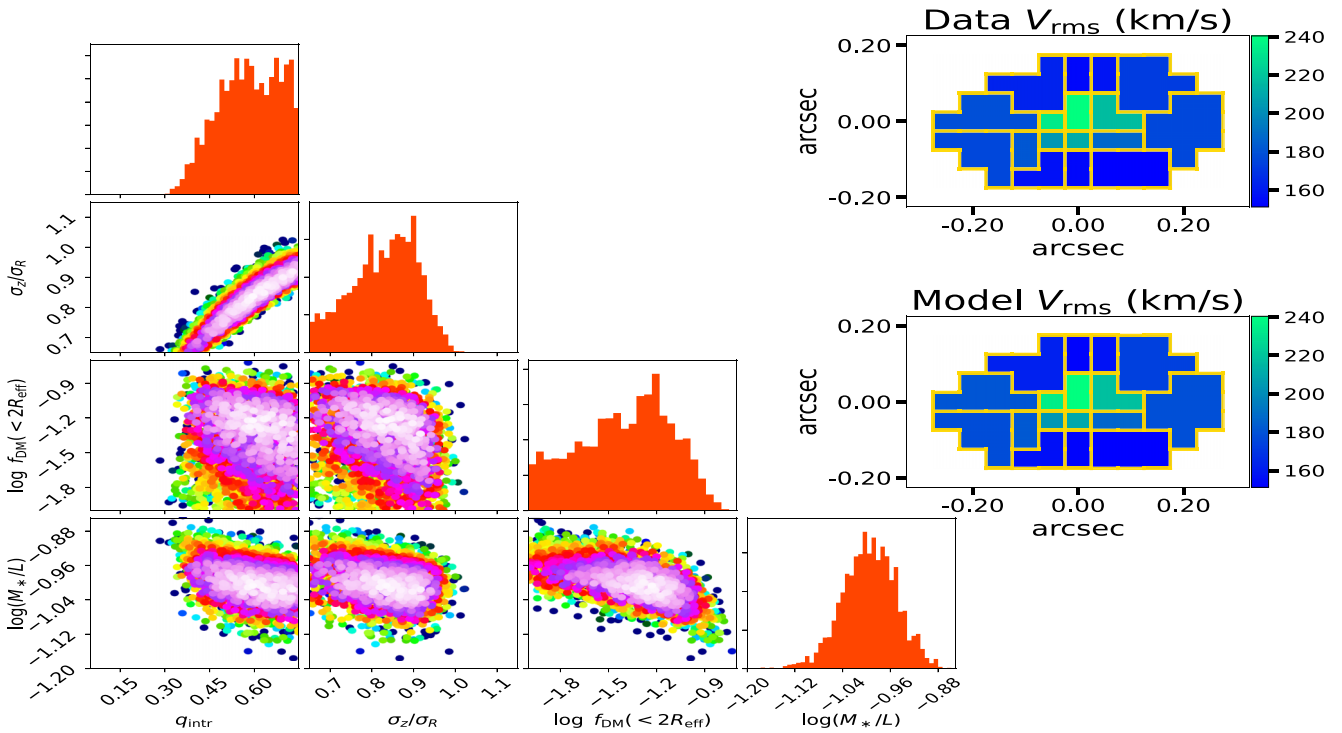

Figure F4. First fiducial model recovery test for $\log f_{\rm DM}(<2R_{\rm eff})$. The tested input value is $\left(\log f_{\rm DM,<2R_{eff}}\right)_{\rm test,in} = -1.25$ and the test output is $\left(\log f_{\rm DM,<2R_{eff}}\right)_{\rm test,out} = -1.22 \pm 0.32$. We have $(\sigma_z/\sigma_R)_{\rm test,out} = 0.835 \pm 0.084$ (in agreement with the input value of 0.85), $q_{\rm test,out} = 0.59 \pm 0.11$ (in agreement with the input value of 0.62), and $\log(M_*/L)_{\rm test,out} = -1.008 \pm 0.044$ (in agreement with the input value of -1.01). In this plot, we denote $\log(M_*/L) \equiv \log\left[(M_*/L)\,/\,(\mathrm{M}_\odot/L_\odot)\right]$.

[1]*Kavli Institute for Cosmology, University of Cambridge, Madingley Road, Cambridge CB3 0HA, UK*
[2]*Cavendish Laboratory – Department of Physics, University of Cambridge, 19 JJ Thomson Avenue, Cambridge CB3 0HE, UK*
[3]*Department of Physics and Astronomy, University College London, Gower Street, London WC1E 6BT, UK*
[4]*Department of Physics, Sub-Department of Astrophysics, University of Oxford, Denys Wilkinson Building, Keble Road, Oxford OX1 3RH, UK*
[5]*International Centre for Radio Astronomy Research (ICRAR), University of Western Australia, 35 Stirling Highway, Crawley, Western Australia 6009, Australia*
[6]*ARC Centre for All-Sky Astrophysics in 3 Dimensions (ASTRO 3D), Australia*
[7]*Max-Planck-Institut für extraterrestrische Physik (MPE), Gießenbachstraße 1, D-85748 Garching, Germany*
[8]*INAF – Osservatorio Astrofisico di Arcetri, largo E. Fermi 5, I-50127 Firenze, Italy*
[9]*Centro de Astrobiología (CAB), CSIC-INTA, Cra. de Ajalvir Km. 4, E-28850 Torrejón de Ardoz, Madrid, Spain*
[10]*Sterrenkundig Observatorium, Universiteit Gent, Krijgslaan 281 S9, B-9000 Gent, Belgium*
[11]*Max-Planck-Institut für Astronomie, Königstuhl 17, Heidelberg, Germany*
[12]*NSF National Optical-Infrared Astronomy Research Laboratory, 950 North Cherry Avenue, Tucson, AZ 85719, USA*
[13]*Steward Observatory, University of Arizona, 933 North Cherry Avenue, Tucson, AZ 85719, USA*
[14]*Max Planck Institute for Astrophysics, Karl-Schwarzschild-Str 1, D-85741 Garching bei München, Germany*
[15]*Ludwig-Maximilians-Universität München, Geschwister-Scholl-Platz 1, D-80539 München, Germany*
[16]*Department of Astronomy, University of Wisconsin-Madison, Madison, WI 53706, USA*
[17]*Institute for Astronomy, University of Edinburgh, Royal Observatory, Edinburgh EH9 3HJ, UK*
[18]*Sorbonne Université, CNRS, UMR 7095, Institut d'Astrophysique de Paris, 98 bis bd Arago, F-75014 Paris, France*
[19]*Scuola Normale Superiore, Piazza dei Cavalieri 7, I-56126 Pisa, Italy*

This paper has been typeset from a TEX/LATEX file prepared by the author.